

Spectrophotometry of HII Regions, Diffuse Ionized Gas and Supernova Remnants in M31: The Transition from Photo- to Shock-Ionization

Vanessa C. Galarza and René A.M. Walterbos¹

New Mexico State University, Department of Astronomy, Box 4500, Dept 30001, Las Cruces, NM 88003

and

Robert Braun¹

Netherlands Foundation for Research in Astronomy, P.O. Box 2, 7990AA Dwingeloo, The Netherlands

ABSTRACT

We present results of KPNO 4-m optical spectroscopy of discrete emission-line nebulae and regions of diffuse ionized gas (DIG) in M31. Long-slit spectra of 16 positions in the NE half of M31 were obtained over a 5-15 kpc range in radial distance from the center of the galaxy with special attention to the annulus of high star formation between 8 and 12 kpc. Slit positions were chosen such that several emission-line nebulae and large sections of diffuse gas could be studied, without compromising the parallactic angle. The spectra have been used to confirm 16 supernova remnant candidates from the Braun & Walterbos (1993) catalog. The slits also covered 46 HII regions which show significant differences among the various morphological types (center-brightened, diffuse, rings). Radial gradients in emission-line ratios such as $[\text{OIII}]/\text{H}\beta$ and $[\text{OII}]/[\text{OIII}]$ are observed most prominently in the center-brightened HII regions. These line ratio trends are either much weaker or completely absent in the diffuse and ring nebulae. The line ratio gradients previously seen in M31 SNRs (Blair, Kirshner, & Chevalier 1981; Blair, Kirshner, & Chevalier 1982) are well reproduced by our new data. The spectra of center-brightened HII regions and SNRs confirm previous determinations of the radial abundance gradient in M31. We use diagnostic diagrams which separate photoionized gas from shock-ionized gas to

¹Visiting Astronomer, Kitt Peak National Observatory, National Optical Astronomy Observatories, which is operated by the Association of Universities for Research in Astronomy, Inc. (AURA) under cooperative agreement with the National Science Foundation.

compare the spectral properties of HII regions, SNRs and DIG. This analysis strengthens earlier claims (Greenawalt, Walterbos, & Braun 1997) that the DIG in the disk of M31 is photoionized by a dilute radiation field.

Subject headings: galaxies: individual(M31) — ism: general — HII regions — supernova remnants

1. Introduction

Our nearest large galaxy neighbor, M31, provides us with an excellent opportunity to study the star-formation process and the properties of the interstellar medium in great detail. This Sb spiral is interesting in that it has a low star formation rate, about $0.2\sim0.5 M_{\odot}/\text{yr}$ (Walterbos 1988), relative to the typical Sb galaxies, which can have star formation rates up to $4M_{\odot}/\text{yr}$ (Kennicutt, Tamblyn, & Congdon 1994). M31’s proximity¹ has inspired numerous studies of its emission-line nebulae both in imaging and spectroscopic mode (e.g. Pellet *et al.* 1978; Blair, Kirshner, & Chevalier 1981; Dennefeld & Kunth 1981; Blair, Kirshner, & Chevalier 1982; Dopita *et al.* 1984a; Walterbos & Braun 1992; Meyssonnier, Lequeux, & Azzopardi 1993; Magnier *et al.* 1995). Due to the large angular size of M31, the spatial coverage of the spectroscopic observations has necessarily been rather limited.

An H α and [SII] 6716,31Å imaging survey of most of the northeast half of M31 resulted in a catalog of 958 gaseous nebulae (Walterbos & Braun 1992, hereafter WB92). The sensitive survey (rms noise $\sim 1.1 \times 10^{-17} \text{ erg cm}^{-2} \text{ sec}^{-1} \text{ pix}^{-1}$) also allowed Walterbos & Braun (1994) to study the diffuse ionized gas (DIG) in this galaxy. This faint component of the ISM, which permeates the disk and can contribute up to 50% of the total H α luminosity of spiral galaxies (see also *e.g.* Ferguson *et al.* 1996; Hoopes *et al.* 1996) remains ill-understood because the ionizing source has not been well constrained. The proximity of M31 facilitates the isolation of gaseous nebulae from the DIG, allowing a direct comparison of their properties.

The WB92 survey also yielded a set of 52 supernova remnant (SNR) candidates, presented in Braun & Walterbos (1993, hereafter BW93), which are generally fainter than the candidates in other M31 surveys such as Blair, Kirshner, & Chevalier 1981 and Magnier *et al.* 1995. To confirm the BW93 SNR candidates, and to further study and compare the

¹Freedman & Madore 1990 determined a distance for M31 ~ 750 kpc based on Cepheid observations; for this work, however, we adopt the traditional value $D \sim 690$ kpc, consistent with the WB92 catalog.

spectral properties of HII regions and DIG in M31, we chose several targets for spectroscopic observation. This paper presents the optical spectrophotometric results of a sample of 44 distinct HII regions, 18 SNR candidates (two of which turned out to be HII regions), and numerous regions of DIG. Greenawalt, Walterbos, & Braun (1997) discussed the global spectral characteristics of the DIG in M31 based on averaged spectra obtained from the same data discussed here. In this paper, we will compare spectra of individual regions of DIG with HII region and SNR spectra.

Details about the observations and data reduction are given in §2. We discuss the extinction corrections in §3. Next we consider the nebular conditions and radial trends in various line ratios for our sample of HII regions in §4. In §5, we discuss the confirmation and radial spectral line variations of the SNRs. This section concludes with a summary of what we can determine about the radial abundance gradient in M31 from the HII region and SNR spectra. It will become clear that while abundance trends are definitely present, line ratio variations due to excitation effects in HII regions and variations in shock conditions in SNRs contribute substantial scatter to the line ratios. We therefore conclude with a comparison of the emission-line properties of HII regions, DIG and SNRs in §6, to shed further light on the ionization mechanism for the DIG. A summary of our results is presented in §7.

2. Observations and Data Reduction

A complete description of the observations and data reduction has already been provided elsewhere (Greenawalt, Walterbos, & Braun 1997); we briefly summarize the important aspects here.

Our long-slit spectra were obtained with the RC spectrograph on the Mayall 4m telescope at Kitt Peak National Observatory in November 1991. The dispersion of the KPC-10A grating we used is $2.77\text{\AA}/\text{pixel}$ which provides a spectral resolution of 6\AA . The total spectral coverage was 3550\AA to 6850\AA with a large overlap region $4000\text{-}6400\text{\AA}$. The dimensions of the slit were $2'' \times 5.4'$, with a spatial scale of $0.69''/\text{pixel}$.

Sixteen different slit positions were obtained on the NE half of M31, concentrated in the three spirals arms between 5 kpc and 15 kpc from the center of the galaxy, with special attention to the annulus of high star-formation activity near 10 kpc. The slit positions on the sky were carefully chosen to obtain at least one HII region, one SNR candidate, and DIG in one slit. Two 15-minute observations were taken at each position with an observation of a nearby standard star in between. These standards aided in the flux-calibration of the

object spectra, which was conducted using the standard IRAF² package techniques. Table 1 provides the following details on the observations: 2D spectrum name which corresponds to the WB92 identification for the most prominent source in the slit (column 1); epoch 2000 right-ascension and declination for slit center (columns 2 and 3); slit position angle on the sky chosen in each case such as not to compromise the parallactic angle (column 4); image field from WB92 where the slit was positioned (column 5); and all WB92 catalog objects for which 1D spectra were extracted (column 6).

The extraction of one-dimensional spectra from the two-dimensional images proceeded as follows. All discrete objects on the 2D spectra were identified on the H α images of WB92. The object boundaries were determined from a comparison of the H α emission-line profile along the slit and a cut across the H α images which most closely corresponds to the position of the slit on the sky. This was not always a straight-forward task because of the difference in spatial resolution between the spectra and the emission-line images, but close matches were obtained after some trial and error. Sky apertures were identified as close as possible on either side of the object apertures and often included the faint emission from nearby DIG. Background sky levels were determined with a first or second order fit in IRAF and subtracted from each object spectrum. The spectra for 50 separate regions of DIG were identified in a similar manner, using apparent morphology and an upper cutoff in emission measure; all DIG extractions have a surface brightness ≤ 100 pc cm $^{-6}$. The DIG spectrum apertures vary from 10 pixels up to 60 pixels.

Many of the large objects in our sample show significant internal structure. We have extracted separate spectra for each of these structures using the H α emission variations as indicators of boundaries. The first spectrum extracted for each nebula contains light from across the entire object in the slit. Subapertures were identified and labelled from left to right across the slit independent of position angle. All the apertures and subapertures are labelled in Fig 1a and Fig 1b. Each structure was classified based on the apparent morphology and light profile in the H α images. We have adopted the classification scheme for the HII regions as published in WB92 with only a few slight variations described further in the Appendix.

Emission-line fluxes were determined by fitting Gaussians to the line profiles with the IRAF routine SPLOT. Uncertainties were estimated by measuring the rms noise on either side of the emission features with an additional 3% flux calibration error based on

²IRAF is distributed by the National Optical Astronomy Observatories, which is operated by the Association for Research in Astronomy, Inc., under cooperative agreement with the National Science Foundation.

the spectra of the standard stars. The fluxes of the emission-lines measured in the overlap region between the blue and red spectra (4000-6400Å) were averaged together. The lines included in this overlap region are H γ , H β , [OIII]4959Å, 5007Å, and [OI]6300Å.

3. Extinction Corrections

The emission lines of HII regions and SNR were corrected for interstellar reddening using the Balmer decrement derived from the observed H α to H β line flux ratio for each spectrum assuming a standard Galactic extinction curve (Savage & Mathis 1979).

The extinction in the faint extended DIG regions was addressed carefully by Greenawalt, Walterbos & Braun (1997). They concluded that assuming a well-mixed dust layer rather than a foreground dust layer produced a difference of less than 10% in the line flux ratios for the average observed Balmer decrement, and we will use the foreground screen model here for the DIG as well as for the HII regions and SNRs. We have assumed the same reddening correction law for the DIG and the HII regions. The intrinsic value of H α /H β was assumed to be 2.86 for the HII regions and DIG, based on Case B recombination and a gas $T_e \approx 10,000$ K (Osterbrock 1989). The SNR H α /H β was taken to be 3.00, the collisional value consistent with shock models of Raymond (1979) and Shull & McKee (1979).

The extinction and other properties of the nebulae are presented in Table 2 and Table 3 for HII regions and SNRs, respectively. Column 3 lists the galactocentric radius for each nebula published in WB92. This radial distance is based on the spiral arm most likely associated with the object as determined by the kinematical model of Braun (1991). Columns (4,5) list the observed H α /H β line ratio and the extinction in magnitudes, A(V). These parameters were used to correct each individual spectrum for interstellar reddening.

The dispersion of A(V) within an HII region can provide important information about the distribution of dust and gas within the nebula. It has been shown that the density within a single HII region is not homogeneous (e.g. Kennicutt 1984). M31 is close enough that our spectra can be used to investigate variations in A(V) across large HII region complexes. By analyzing emission from a cross-cut of an entire HII complex, we are no longer biased by selecting only the bright, hence possibly less extinguished sections of the HII region. We can thus investigate if single extinction values derived for more distant extra-galactic HII regions could be in error due to significant extinction variations across the complexes.

In a recent study of HII regions in M33 and M101, Petersen & Gammelgaard (1997) found that the variation of A(V) within large HII region complexes was typically 0.3

magnitudes or less and that the extinction values usually increased toward the edges of the nebulae. We conducted a similar exercise for the largest HII regions in our sample. Fig 2 shows the $A(V)$ variation within HII regions complexes with more than 3 aperture extractions. The extinction obtained from each subaperture is plotted along with the $H\alpha$ profile of the entire complex within the slit.

We note several points. Not surprisingly, the extinction measured for the brightest region of a complex tends to be close to the derived average extinction for that complex, a consequence of luminosity weighting that is occurring in deriving an average extinction. However, the brightest regions in a complex are not necessarily the ones with the least extinction (e.g. K703, K525). This is important, because if they were, then the derived average extinctions for complexes would be systematically underestimated as a result of this luminosity weighting. Typical variations in extinction across a complex amount to ± 0.5 mag. While this is not negligible, this variation is less than that observed in the HII region population as a whole (panel g in Fig 2). There is a faint region in the complex K703 which apparently has significantly higher extinction than the rest of the complex (by 2 mag). In the present small sample, however, it is the only such region and it is therefore not clear how common such variations are.

The peak in the distribution of $A(V)$ (Fig 2g) for our sample is 0.8 magnitudes. The observed average foreground extinction toward M31 is about 0.25 V mag (Burstein & Heiles 1984, Walterbos & Schwering 1987). The excess must be due to internal extinction in the disk of M31. The peak in our distribution is only slightly lower than the peak of the whole WB92 catalog of 958 nebulae, which was near 1.0 mag. The extinction corrections in WB92 were determined by estimating of the amount of atomic hydrogen gas present in front of each object. Our extinction values, based on Balmer decrements obtained from spectra, are much more accurate. While there is overall agreement in the measured range of extinctions derived here and in WB92, the agreement for individual objects is poor, which is not surprising given that the WB92 method only provides a statistical estimate of the extinctions. We find no clear trends in $A(V)$ with observed $H\alpha$ intensity, but we do observe the highest measured extinctions in the annulus of vigorous star-formation between 8 to 12 kpc, where the gas distributions also peak (e.g. Walterbos 1988).

4. HII Regions

We have spectra for 46 separate HII regions from the WB92 catalog of the NE half of M31; this includes two spectroscopically rejected SNR candidates which have been reclassified as faint HII regions. The spatial distribution of these nebulae is concentrated in

the high star-formation 10 kpc spiral arm, with the fewest number of objects observed at the inner 5 kpc ring. This makes the study of radial trends, including the determination of the chemical abundance gradient more uncertain. However, we have observed some correlations between line ratios and position in the galaxy as well as spectral differences between nebulae of different morphologies. These are presented in §4.2, while the next section discusses the morphological classification of the HII regions.

4.1. $\text{H}\alpha$ Morphology

The general properties of our HII region sample are shown in Fig 3. Average emission measures for each object were determined from the reddening corrected total $\text{H}\alpha$ fluxes for each nebula using the spectroscopically derived $A(V)$ and the sizes given in WB92. The nebular diameters are the average of D_{major} and D_{minor} quoted in WB92. The average electron density, $n_{e,\text{rms}}$, is derived from the corrected $\text{H}\alpha$ emission measure assuming unit filling factor ($\text{E.M.} = \int n_e^2 \, dl$). It was also assumed that the HII regions are spherically symmetric on average such that the path length through the nebula along the line of sight is the same as the apparent linear size. It has been noted (Kennicutt 1984) that these are unrealistic assumptions; we merely want to demonstrate the range in properties in comparison to other HII region samples. The dotted lines in this plot represent lines of constant emission measure.

The point types used in Fig 3 distinguish between the morphological classifications given in the WB92 catalog: center-brightened compact (shown as triangles), diffuse (five-pointed stars) and rings (open circles). We have also included the large HII region complexes in these plots, shown as open squares. The plot shows that a rather smooth trend exists from the lower surface brightness extended objects to the compact sources. The distinction between the compact sources and the extended objects is much greater than between the diffuse, ring and HII region complexes. This separation also appears in the spectral properties of the objects, as is shown in the next section.

4.2. HII Region Emission-Lines and Nebular Conditions

The most prominent HII region emission-line fluxes corrected for interstellar reddening are presented in Table 4 in the form of line ratios with respect to $\text{H}\beta$ or $\text{H}\alpha$. Columns (1,2) list the name of the object as designated in the WB92 catalog plus cross-references to Pellet *et al.* (1978) objects, and the aperture sequence label. The other columns list the extraction

aperture width in arcseconds (column 3), the H α emission measure for the region within the spectrum corrected for interstellar reddening (column 4), and corrected line flux ratios: [OII]3727Å/H β (column 5); [OIII]5007Å/H β (column 6); [NII]6548,83Å/H α (column 7); and [SII]6717,31Å/H α (column 8). The assigned morphology is listed in the final column of Table 4. We have used a similar classification for the subapertures as that used for the discrete nebulae in WB92 with a few modifications; see the Appendix for a complete description. Faint emission lines rarely found in M31 HII regions were also detected in a few of our objects. These features include the [NeIII] forbidden lines and He I recombination lines. The extinction corrected fluxes for these lines are listed in Table 5.

Electron temperatures and densities were derived from the appropriate optical emission line ratios using the Lick Observatory FIVELEV code (De Robertis, Dufour, & Hunt 1987) and recently updated atomic data. Columns (6,7) in Table 2 list the density sensitive [SII] line ratio and the derived n_e (cm $^{-3}$) for the HII regions. Most of our objects are in the low density limit and only two objects had marginally detectable [OIII]4363, required to determine T_e (Osterbrock 1989). The electron temperatures were estimated at $T_e \sim 16,500\text{K} \pm 4,000\text{K}$ for K87 and $T_e \sim 9,000\text{K} \pm 1,000\text{K}$ for K932. A canonical HII region temperature of 10 4 K was assumed for all other objects.

While the HII regions show emission-line ratios within the range predicted by photoionization models, we do observe some spatial variations in line flux even within the limited galactocentric radius sampled by our data. These variations are likely due to the chemical abundance gradient in the disk of the galaxy but may also reflect differences in the ionization level and excitation between nebulae at different radii.

Due to the large inclination of the disk of M31, the galactocentric radii of most of our objects are uncertain. In order to study the effects of uncertain position in the galaxy, we have considered three radial distance determinations in studying the spectral variations. The first and least accurate distance (D_1) is determined by assuming that the disk of M31 is an infinitely thin disk projected an inclination angle of 77°; the radial distances are based on the x-y positions of the objects in this coordinate system. The M31 kinematical model of Braun (1991) provides two possible distance measurements (D_2 , D_3), based on fitting spiral arms to the HI kinematics; WB92 lists these values as the position of the first and second most likely spiral arm associated with each source.

As is apparent in all the radial plots that follow, line ratio trends with radius are, with some exceptions, marginal or not seen at all. The plots show a lot of scatter even at a single radius. While all the radial plots were created using each of the possible distance measurements, we have chosen to show only the plots based on D_2 which show radial gradients with the least scatter. Undoubtedly, some of the scatter in these plots is still

likely due to the uncertainty in the radial distance. However, much of the scatter is real and presents an important problem in the interpretation of radial gradients in emission-line ratios, as has been pointed out by Blair & Long (1997). For example, the scatter may be caused by internal variations in temperature, excitation or density. Most of the data points are based on small sections of nebulae that are already modest in luminosity to begin with. If the HII regions can be ionized by just a few massive stars, the presence or absence of just one bright O star can significantly affect the spectrum. These effects are discussed more in Section 6. A line was fit to the data points in each plot, using a weighted least squares method. The fits are shown only if the resulting slope differed significantly from 0, and if the correlation coefficient exceeded 0.5.

The first set of radial diagrams shows the variation of three oxygen line ratios: $[\text{OIII}]5007\text{\AA}/\text{H}\beta$ (Fig 4a-d), $[\text{OII}]3727\text{\AA}/[\text{OIII}]5007\text{\AA}$ (Fig 4e-h), and R_{23} (Fig 4i-l) defined by Edmunds & Pagel (1984) as the ratio of the sum of $[\text{OIII}]\lambda 5007\text{\AA}$, $[\text{OIII}]\lambda 4959\text{\AA}$, and $[\text{OII}]\lambda 3727\text{\AA}$ with respect to $\text{H}\beta$. The size difference in the symbols used indicates if the data are from a discrete object (large size) or a subaperture of an extended object or HII region complex (small size). This distinction is almost equivalent to a luminosity coding of the data points.

The line ratio $[\text{OIII}]5007\text{\AA}/\text{H}\beta$, the excitation parameter (η), essentially measures the hardness of the radiation field within the ionized nebula or equivalently, the temperature of the central OB star(s). This line ratio is also sensitive to chemical composition (Searle 1971). An outward radial increase in $[\text{OIII}]/\text{H}\beta$ has been known to exist in disk galaxies for some time (Aller 1942 and Searle 1971) and is commonly used as evidence for an oxygen abundance gradient in disk galaxies (Scowen, Dufour, & Hester 1992; Zaritsky, Hill, & Elston 1990). However, a strict empirical correlation between chemical abundance and the observed $[\text{OIII}]5007\text{\AA}/\text{H}\beta$ line ratio is debatable since the line ratio only measures one ionization state of oxygen (Edmunds & Pagel 1984; Zaritsky 1992). For M31, the expected increase in excitation with galactocentric distance shows up only in the compact HII regions. The diffuse nebulae, ring segments and DIG do not reproduce this trend and appear only to scatter in the range covered by the compact sources.

The high surface-brightness compact nebulae show a decrease in the line ratio $[\text{OII}]/[\text{OIII}]$ with increasing distance from the center, as observed in HII regions in other galaxies. The extended objects and DIG again appear to show mostly scatter. While the $[\text{OII}]/[\text{OIII}]$ ratio gives some information about the level of ionization in a nebulae, it is also affected by metallicity. To properly study the ionization of HII regions, one would need to sample the multiple ionization states of another element, like sulfur, but this requires spectral coverage to the infrared ($[\text{SIII}]9069\text{\AA}$ and $[\text{SIII}]9532\text{\AA}$).

The R_{23} parameter has been suggested as a good probe of oxygen abundance in cases where the electron temperature, T_e , cannot be determined directly from observations (Pagel *et al.* 1979). Several calibrations of this line ratio with oxygen abundance have been published (Pagel, Edmunds & Smith 1980; Edmunds & Pagel 1984; Vilchez 1989) including the use of a weighted sum of the [OII] and [OIII] lines (Binette *et al.* 1982). Radial trends in the R_{23} ratio have been observed and studied extensively in many nearby galaxies (Evans 1986; Henry & Howard 1992; Garnett *et al.* 1997; Kennicutt & Garnett 1996). We find a similar trend in our M31 data, although it again only appears in the center-brightened nebulae.

We studied the luminosity dependence of the oxygen emission-line ratios with position in the galaxy to see if the lack of radial trends and the large amount of scatter at any given radius could be explained by differences in the number of ionizing stars within the nebulae. Encoding the data points with the integrated luminosity of the nebula from which the aperture was extracted indeed strengthens the radial trends in the compact objects but has little effect on the scatter observed in the other objects.

The radial plots of [NII]6583Å and [SII]6716,31Å relative to H α are shown in Fig 5. There appears to be a decreasing trend towards the outer disk of M31 in the [NII]/H α ratio in the lower surface brightness objects only. We will come back to this in the discussion of the SNR spectra (§5.2 and §5.3). For the bright compact HII regions, no such trend is observed, possibly because a significant fraction of the nitrogen may be doubly ionized there.

The radial distribution of H α surface brightness of the object sections for which we have obtained spectra is shown in Fig 5i-1. This figure shows that the observed emission-line ratio trends discussed above are not caused by a correlation between H α surface brightness and radial distance. We believe the observed trends in oxygen and nitrogen are the consequence of the chemical abundance gradient in M31 (see §5.3).

5. Supernova Remnants

5.1. Confirmation of Candidates

One of the original goals of this project was to spectroscopically confirm the supernova remnant candidates from the BW93 catalog. This catalog consists of 52 SNR candidates which were identified by high [SII]/H α line ratios ($[\text{SII}]/\text{H}\alpha > 0.45$) in the narrow-band images published in WB92. Several of these candidates coincide with SNR candidate objects in other catalogs such as Blair, Kirshner, & Chevalier (1981, hereafter BKC81) and

Magnier *et al.* (1995). A recent attempt has been made to confirm SNR candidates using the ROSAT HRI (Magnier *et al.* 1997). Less than 10% of the optically identified candidates were detected in the X-ray, however. This can be explained as the result of a very tenuous interstellar medium in the vicinity of SNR in M31, with typical densities less than 0.1 cm⁻³. Thus, it is quite difficult to confirm the candidates using X-ray emission alone and optical spectroscopy continues to be the necessary and preferred method of identifying these objects in M31.

Table 6 lists the spectral line ratios for all SNR candidate spectra. Included in this table are the object name plus cross-reference to BKC81 and Blair, Kirshner & Chevalier (1982, hereafter BKC82) and aperture sequence label in Columns (1,2), aperture width in arcseconds in Column (3), and reddening corrected H α emission measure in Column (4). Columns (5-9) list the reddening corrected flux ratios of [OII]3727Å and [OIII]5007Å to H β and [OI]6300Å, [NII]6548,83Å and [SII]6716,31Å to H α .

To address the candidacy of our objects, we first compared the observed spectroscopic [SII]/H α line ratio with the ratio obtained from the narrow-band line images for the exact object section captured in each spectrum. In all but a few rare cases, there is a good agreement between the spectral ratio and image ratio. Bad pixels in the line images or in the 2D spectra images affected the agreement in a few cases; poor signal-to-noise also played a factor for a few candidates.

The morphology of the candidates studied here include discrete ring-like structures, faint diffuse nebulae and compact sources embedded in nebular complexes (indicated by an 'A' in the object name). Most of the SNR extractions show enhanced [OII]3727Å and [OIII]5007Å emission, and a few of the objects show a bright [OI]6300Å feature in their spectra. These factors taken together help in the confirmation of these candidates. In several cases, the gas surrounding embedded compact SNR candidates does not show enhanced [SII] emission relative to H α . Two SNR candidates (K310 and K446) were rejected as supernova remnants due to low [SII]/H α and lack of bright [OIII] emission. It is suspected that these objects are in fact HII regions. SNR candidates of particular interest are described in the Appendix.

5.2. SNR Line Ratios and Nebular Conditions

The brightness of optical emission lines in shocked gas depends on multiple factors: the electron density and electron temperature in the post-shock region which are related to the velocity of the shock front; the density of the medium into which the shock is propagating;

and the chemical abundance of elements of the swept up material, among other things. The modelling of these effects on the optical spectra of SNR has been carried out by Dopita, Mathewson & Ford (1977), Shull & McKee (1979), and Raymond (1979). Through a series of diagnostic diagrams based on the ratios of optical emission lines, it has been shown that the variations in the spectra of SNRs are due primarily to the chemical abundance effects and only minimally to the shock conditions for shock velocities near and above 100 km s^{-1} (Dopita *et al.* 1984a). However, the modelling of interstellar shocks is not straightforward due to the large number of variables involved and the theoretical models do not always agree with observations. There are many complications due to the depletion of volatiles onto grains, the destruction of grains and even magnetic field effects. However, there are several basic line ratio diagnostics which can help probe the physical conditions of the shocks.

BKC82 have used the variation in the observed line flux ratios of SNR to derive the abundance gradient in the disk of M31. The spatial distribution of our confirmed candidates is limited to the outer regions of the disk and we have no objects at galactocentric radii smaller than 8kpc. Thus we cannot use our data to directly measure the abundance gradient in M31. However, the general radial trends found by BKC82 are fairly well reproduced with our new data. For comparison, we have plotted the BKC82 data points (in open squares) as well as our confirmed SNR data points (solid squares) in Fig 6. The agreement in the slopes and also in the scatter is good given the faintness of most of our remnants relative to those studied by BKC82.

Fig 6a shows the radial variation of the excitation line ratio $[\text{OIII}]5007\text{\AA}/\text{H}\beta$ for SNRs. Contrary to the trend found in the HII region spectra, the SNR spectra do not show a clear increase in excitation with distance from the center, though there is significant scatter in the ratio at any given position. Since the [OIII] emission arises from a region very close to the shock front, two competing factors govern the brightness of the [OIII] lines: the postshock temperature (equivalent to shock velocity) and the oxygen abundance (Dopita 1977). The ionization line ratio, $[\text{OIII}]5007\text{\AA}/[\text{OII}]3727\text{\AA}$, on the other hand, has been shown to be more sensitive to the postshock conditions and less sensitive to metallicity (Dopita 1977). Our data in Fig 6b show fair agreement with the BKC points with more scatter, likely due to measurement error. These two emission line ratios do not likely indicate a chemical abundance gradient, but reflect a gradient in the SNR physical conditions across the galaxy.

Our SNR data also show the correlation between [OII] and [OIII] emission found by BKC82 (Fig 6c). The curves plotted here are shock model predictions for metallicity variations (thick solid curve), shock front velocity variation (dash-dot curve) and shock velocity variation with the pre-ionization of the medium (dash curve) taken from Dopita

et al. (1984). The behavior of the two oxygen line ratios can be reproduced by varying the abundance of oxygen relative to hydrogen (by number) but not by varying the shock conditions. This indicates that the group of SNRs studied here do show a wide range of oxygen abundance.

The [NII]/H α trend shown in Fig 6d shows the cleanest radial trend. The [NII] lines are not strongly affected by shock temperature since they originate in the large recombination region behind the shock front. These lines are also not affected by collisional de-excitation and so are relatively insensitive to electron density. This trend must be a direct result of the abundance gradient in M31. The [SII]/H α gradient (Fig 6e), may also primarily show an abundance effect.

The physical conditions derived from the optical spectra for our sample of SNRs are listed in Table 3 (density sensitive [SII] line ratio and n_e in Columns (6,7) respectively) and Table 7 (T_e). Electron densities were determined for those regions with good [SII] doublet line detections ([SII]6716Å/[SII]6731Å within the theoretical limits) using the Lick Observatory FIVEL program with the assumption that the recombination zone from which the sulfur doublet lines arise has a temperature of 10⁴K. In most cases, the SNRs are in the low density limit. This has been recently confirmed by X-ray data which show that upper limits to the electron density in the interstellar medium in the vicinity of SNR candidates in M31 is about 0.1 cm⁻³ (Magnier *et al.* 1997).

Unlike HII regions, the conditions in the postshock gas of SNR are such that the high excitation emission-line [OIII]4363Å is easier to detect. This line was detected in a few of our SNR candidates spectra, allowing the determination of T_e . Using the formalism of Kaler *et al.* (1976) and the [OIII]4959Å + 5007Å/[OIII]4363Å emission-line ratio, we have determined the temperatures listed Table 7.

In Fig 6f, we plot the electron temperatures derived for the SNR with available [OIII]4363Å measurements as a function of radial distance. Our data points are in fair agreement with the BKC82 points at radii near 10kpc. There are too few points in the outer regions of the galaxy to see a spatial correlation in the post-shock temperature in the galaxy. Such a correlation would explain the slight increase of the [OIII]/H β and [OIII]/[OII] line ratios towards the center of the galaxy shown in Fig 6a and 6b.

5.3. Summary of abundance trends in HII regions and SNRs

Despite our limited radial sampling of the disk of M31, we have detected radial trends in some of the emission lines for both HII regions and SNRs which likely reflect the abundance

gradient in M31. We compare our results, which concern mostly low-luminosity objects, with those of BKC81 and BKC82 who concentrated on the brightest objects and covered a larger radial range. Dopita *et al.* (1984) reanalyzed the Blair *et al.* data with improved shock ionization models, to resolve a discrepancy in the derived oxygen abundances for HII regions and SNRs.

The oxygen line ratios $[\text{OIII}]/\text{H}\beta$, $[\text{OII}]/[\text{OIII}]$, and R_{23} observed in the center-brightened HII regions (Fig 4a, 4e, 4i) show the expected correlation with radial position within the galaxy. These line ratios are all consistent with increasing metallicity towards the center of the galaxy. The gradient we can infer from the R_{23} parameter is -0.06 ± 0.03 dex kpc^{-1} , in fair agreement with the gradient derived from HII region spectra by BKC82 and the gradient based on shock-ionization modeling of SNR line ratios (Dopita *et al.* 1984), -0.05 ± 0.02 dex kpc^{-1} . Peculiarly, none of the other types of HII regions show a strong radial gradient in the oxygen emission lines.

The correlation between the $[\text{OII}]$ and $[\text{OIII}]$ emission from the SNRs (Fig 6c) indicates that these objects also exhibit metallicity differences (Dopita *et al.* 1984). The radial distribution of $[\text{OII}]/\text{H}\beta$ and $[\text{OIII}]/\text{H}\beta$ observed in our sample of SNRs is in good agreement with the line ratios found in BKC82 sample of SNRs. This further confirms the oxygen abundance gradient determined from the proper shock-ionization treatment of the BKC82 SNR emission lines by Dopita *et al.* (1984).

The center-brightened HII regions do not show a radial gradient in $[\text{NII}]/\text{H}\alpha$ over the range 5 to 15 kpc (see Fig 5), consistent with BKC82, who mainly show higher ratios for this line within 5 kpc from the center. However, the $[\text{NII}]/\text{H}\alpha$ ratios are correlated with radial distance in the case of the ring-like nebulae which show a gradient in $[\text{NII}]/\text{H}\alpha$ (Fig 5) of -0.02 ± 0.01 dex kpc^{-1} ; the diffuse nebulae and the DIG also show this trend, but with more scatter. The photoionization models for these low-excitation regions (e.g. Domgörgen & Mathis 1994) indeed show the line ratio of $[\text{NII}]/\text{H}\alpha$ to correlate with the nitrogen abundance. These authors note that the forbidden line ratios depend on electron temperature and abundance in complicated ways, but their calculations show a monotonic pattern for $[\text{NII}]/\text{H}\alpha$, while the $[\text{SII}]/\text{H}\alpha$ model ratio trends in Domgörgen & Mathis (1994) with abundance seem to be more complex. This may explain why our data do not show a radial trend in $[\text{SII}]/\text{H}\alpha$ ratios. In comparison, the SNRs show a steeper gradient of -0.04 ± 0.01 dex kpc^{-1} in the $[\text{NII}]/\text{H}\alpha$ line ratio (Fig 6d). This discrepancy, although not explicitly noted by BKC82, can be reproduced using their HII region and SNR data. Both the average value of the $[\text{NII}]/\text{H}\alpha$ line ratio and the radial gradient of this line seen in the SNR and the HII regions differ significantly. However, the methods used to determine the nitrogen abundance in the photoionized nebulae and the shock-ionized nebulae are distinct,

so despite differences in the line flux ratios, the nitrogen abundances derived from both types of objects are consistent with each other (BKC82). Our ring-like and diffuse nebulae, and SNR line ratios are consistent with the HII regions and SNRs in BKC82, so we confirm the abundance gradient published previously for the nitrogen in M31, approximately -0.07 dex kpc^{-1} .

6. Discussion

The optical spectra of HII Regions, SNRs, and regions of DIG make it possible to compare the emission-line properties of these different classes of objects. Diagnostic line-ratio diagrams are a good way to constrain the ionization and excitation properties of various phases of the ISM. This type of spectral analysis is especially important in the case of the DIG where the ionization mechanism has not been well constrained. We consider observed line ratio trends with $\text{H}\alpha$ surface brightness, present diagnostic diagrams which separate stellar photoionized from shock-ionized nebulae, and discuss how a smooth transition between HII regions and DIG is indicated.

6.1. Spectral Line Transitions: HII Regions and DIG

As noted by several authors (Martin 1997; Wang, Heckman & Lehnert 1997; Greenawalt, Walterbos & Braun 1997), there is a strong correlation between the $[\text{SII}]/\text{H}\alpha$ line flux ratio and the $\text{H}\alpha$ surface brightness for HII regions and DIG. Is such a trend present for other forbidden lines as well?

The four panels of Fig 7 show the line ratio variations with $\text{H}\alpha$ emission measure in HII regions and DIG for $[\text{OIII}]/\text{H}\beta$, $[\text{SII}]/\text{H}\alpha$, $[\text{NII}]/\text{H}\alpha$, and $[\text{OII}]/\text{H}\beta$. Errorbars have only been included for the DIG to reduce clutter; errorbars for the HII region data are typically much smaller due to higher signal-to-noise.

No systematic variation is observed in the $[\text{OIII}]$ emission with changing surface brightness in either the HII regions or in the DIG. In fact, the DIG $[\text{OIII}]$ emission is comparable to that of HII regions. In the Wang, Heckman & Lehnert (1997) scenario which proposes the existence of two types of DIG, this suggests that we may be mostly seeing diffuse gas which resides in the plane of the galaxy and is associated with star-formation. Strong $[\text{OIII}]$ emission would be consistent with a second type of DIG, a disturbed phase which may exist higher above the plane of disks galaxies and may be shock-ionized (Wang, Heckman & Lehnert, 1997; Rand 1998). Of course, the relatively edge-on orientation of M31

might hide the faint emission from this gas far above the midplane of the galaxy, but there are other reasons to believe that M31’s DIG layer is not very thick (Walterbos & Braun 1994). We have already mentioned that the [OIII] emission from the center-brightened HII regions varies as a function of position in the galaxy due to the metallicity gradient in M31. This increase is not seen in the DIG surrounding these HII regions (see §3.3), which may explain why there is less scatter in this ratio for the DIG than for HII regions.

The strongest correlation observed to date is the relative increase in the [SII] emission with decreasing $H\alpha$ surface brightness (Fig 7b). The [SII]/ $H\alpha$ ratio has commonly been used as one of the defining characteristics separating HII regions and DIG, the first being the low surface brightness in $H\alpha$ for the DIG, coupled with diffuse morphology. Most HII regions have [SII]/ $H\alpha$ ratios below 0.3 while the DIG has ratios which reach up to 1.0. The interesting point about this plot is the positioning of the diffuse and ring nebulae relative to the center-brightened sources and the DIG. These points seem to fill the gap between the two brightness extremes creating a smooth sequence in the [SII]/ $H\alpha$ ratio. The extended nebulae may be ionized by a more diffuse radiation field than the center-brightened sources. Thus the smooth trend observed in this plot is likely the result of a smoothly decreasing ionization parameter from the compact sources down to the most diffuse ionized gas. This trend is reproduced in the fainter [NII] emission (Fig 7c) albeit with much more scatter than the [SII] lines. In this case, abundance effects may play a role in the scatter.

As is the case for [OIII], the [OII] emission (Fig 7d) is not strongly correlated with $H\alpha$ emission measure in the HII regions or the DIG. One might have naively expected to see the same increasing trend with decreasing $H\alpha$ emission measure in all emission lines arising from singly-ionized species if the increase in flux is due to a decreasing ionization parameter. However, the photoionization models of Domgörzen & Mathis (1994) predict that only the [NII] and [SII] flux will increase as the ionization parameter decreases. The [OII] emission is nearly independent of the ionization parameter and thus remains fairly constant in the HII regions and in the DIG.

6.2. Diagnostic Diagrams: HII Regions, SNR and DIG

Over the last two decades, theoretical modeling of the emission line spectrum of ionized gas has proven quite useful in determining various characteristics of the gas. Line ratio diagnostics of excitation conditions were investigated by Baldwin, Phillips & Terlevich (1981, hereafter BPT81), resulting in a set of diagrams which separate photoionized gas from shock-ionized gas. Evans & Dopita (1985) developed a set of solar metallicity HII region grids on these diagrams to study the effects of varying the stellar ionization temperature

T_{ion} , the mean ionization parameter $\bar{Q}(H)$, and the element-averaged metallicity \bar{Z} . These grids are based on photoionization models for steady-state spherically symmetric nebulae with unit filling factor and a centrally located OB association, all assumptions which do not necessarily hold in real HII regions. However, observational data on HII regions fit quite nicely into these grids showing relatively good agreement between known conditions and those predicted by the models.

Here we use recent ionization models which predict line ratios for various ionization mechanisms, ionization parameters and nebular conditions (eg. Shields & Filippenko 1990; Sokolowski 1993; Domgörden & Mathis 1994) on these diagnostic diagrams to study the differences in the spectra of the different types of HII regions, DIG and SNRs. Although in all cases we have used reddening corrected line ratios, one of the advantages of diagnostic diagrams is that most of the ratios used are based on lines very near in wavelength so errors in the reddening correction will not affect our results.

The first set of diagnostic diagrams compares the [OIII] and [NII] emission to the [SII] emission in the HII regions, DIG and SNR. The group of data points clearly shifts towards higher [SII]/H α in each consecutive panel (Fig 8a-d). The center-brightened HII regions fall completely within the photoionization model box (labelled as “HII region”) of Shields & Filippenko (1990) while the diffuse and ring-like nebulae begin to scatter outside this box towards shock ionization models (labelled as “LINER”). The DIG and SNRs are found well within the box for shock-ionization with very few exceptions. Although the [SII] emission from the DIG is inconsistent with the photoionization models of Shields & Filippenko (1990), the predictions of Sokolowski (1993) and of Domgörden & Mathis (1994) which specifically addressed photoionization by a dilute radiation field, do reproduce the enhancement of the [SII] emission in the lower emission measure gas. The arrows on the model curves indicate the direction of decreasing ionization parameter.

The [NII] and [SII] emission features can be used together to best separate photoionization and shock-ionization mechanisms (Fig 8e-h). All confirmed SNR in our data have by definition [SII]/H α ≥ 0.45 , so we have divided up each of the plots by a dashed line at $\log([SII]/H\alpha) = -0.35$. From the plots, it is apparent that there also seems to be a lower limit on the [NII] emission of the shock-ionized nebulae near $\log([NII]/H\alpha) = -0.3$. We have placed a dashed line at this value to split up each plot into four quadrants. Only the SNR occupy the upper right corner while the HII regions and DIG are found mostly outside of this quadrant. The two Domgörden & Mathis (1994) models (“leaky” and “composite”) are in fair agreement with the observed spectra of the DIG, showing the increase in [NII] with a more rapid increase in the [SII] emission as the ionization parameter decreases.

Two classic BPT81 excitation plots based on the ionization line ratio [OII]/[OIII]

are given in Fig 9. The first set of panels shows the correlation between $[\text{OIII}]/\text{H}\beta$ and $[\text{OII}]/[\text{OIII}]$. The center-bright HII regions lie completely below the upper envelope of photoionization models (Evans & Dopita, 1985). The diffuse and ring nebulae show a bit more scatter which places a few points above this curve. The one point lying far above this curve corresponds to the bright ring segment, K450.a which shows extraordinarily high reddening due to a very weak $\text{H}\beta$ flux. The DIG (Fig 9c) also lie mostly below this curve, suggesting the oxygen line ratios are consistent with even the simplest photoionization models. The Domgörßen & Mathis (1994) models at the higher ionization parameter predict the $[\text{OIII}]$ emission fairly well.

The SNRs (Fig 9d) cluster about the upper photoionization curve with most points lying above the curve, as expected, although the number of points lying below the theoretical curve is substantial. The $[\text{OIII}]$ emission in a SNR is sensitive to both the shock velocity and chemical abundance, as has already been pointed out, so the points below this curve are not necessarily consistent with photoionization model predictions.

Placing our data points in the $[\text{NII}]\text{6584}/\text{H}\alpha$ versus $[\text{OII}]/[\text{OIII}]$ plane (Fig 9e-h) also separates the two ionization mechanisms. The dashed-line boxes represent theoretical models for photoionization and shock ionization based on Shields & Filippenko (1990). As in previous plots we also show the models of Domgörßen & Mathis (1994). Although the center-brightened nebulae show a wide range in the ionization ratio, the $[\text{NII}]$ emission remains fairly constant around the typical HII region value of $\log([\text{NII}]/\text{H}\alpha) \approx -0.4$. The DIG, diffuse and ring-like HII regions (in Fig 9b and 9c) show a similar distribution consistent with photoionization with only a few points scattering into the shock model regime.

However, the SNRs cluster about an average value of $\log([\text{NII}]/\text{H}\alpha) \approx -0.2$, forcing the points to lie in the shock-ionization box. Again, there are numerous SNRs which lie below the shock-ionization model box and there appears to be even more overlap between the SNRs and the HII regions than in Fig 9a-d. This is most likely an abundance effect, since the $[\text{NII}]$ lines in SNRs are sensitive to chemical composition not the shock conditions. The SNRs which fall below $\log([\text{NII}]/\text{H}\alpha) = -0.2$ still show the elevated $[\text{SII}]$ emission expected from shock conditions as is shown in Fig 8h.

Analysis of the emission-line diagnostic diagrams leads to the following conclusions:

- The enhanced $[\text{SII}]$ emission from the DIG are the only forbidden lines not clearly reproduced by simple photoionization models, that would seem to be more consistent with shock-ionization. However, dilute photoionization models such as those presented by Domgörßen & Mathis (1994), do explain the enhanced $[\text{SII}]$ emission while keeping

the [NII], [OII], and [OIII] line strengths near the values found in typical HII regions. The optical emission lines from the DIG observed thus far in M31 are consistent with the low ionization parameter photoionization models as described in Greenawalt, Walterbos, & Braun (1997).

- The diagnostic diagrams presented here separate the spectroscopically confirmed SNRs from the photoionized nebulae fairly well, the best case being that of the [NII]/H α vs. [SII]/H α plot (Fig 8). The shock-ionized nebulae exist in a very restricted quadrant of this plot with enhanced [SII] and [NII] emission. The DIG does not occupy this quadrant.
- The line ratios for the diffuse HII regions and the ring nebulae are consistent with photoionization models and form a transition between center-brightened HII regions and the DIG in terms of the [SII]/H α ratio.

7. Summary

We have obtained deep optical spectroscopic observations for 46 HII regions (including 2 rejected SNRs), 16 confirmed SNRs, and numerous regions of diffuse ionized gas in M31. The majority of the HII regions studied here are in the low density limit and have low enough temperatures that direct determination of T_e by the observation of the [OIII] 4363Å line is impossible. This complicates the determination of the abundance gradient in M31, although the observed variations of the line ratios with radius indicate that a gradient does exist. The abundance gradient we determine for M31 based on the R_{23} parameter is -0.06 ± 0.03 dex kpc $^{-1}$, consistent with all previously determined values.

This radial variation of line ratios does appear to depend on morphology. The higher surface brightness HII regions show spectra which are dominated by local chemical abundance effects and thus can be used to trace out the chemical gradient in the galaxy. The spectra of the diffuse and ring HII regions do not show radial line ratio trends and appear to be dominated by ionization and excitation effects rather than metallicity.

We have confirmed 16 of the 18 observed SNR candidates from the BW93 catalog. The two remaining objects were rejected due to low [SII] emission. These objects also do not show enhanced [OIII] or [OI] emission in their spectra and were thus reclassified as normal HII regions. The radial trends in the line ratios for the confirmed SNR agree with previously published results (BKC81 and BKC82).

While the [SII] emission from the HII regions and DIG shows a strong increase with

decreasing $\text{H}\alpha$ emission measure, no other spectral feature exhibits such behavior. The smooth transition in $[\text{SII}]/\text{H}\alpha$ seen from the center-brightened HII regions to the DIG strongly suggests that the DIG is affected by a lower ionization parameter, diluted radiation field. The diffuse and ring-like HII regions which exhibit strong ionization and excitation effects in their optical spectra, represent transitional objects between the bright HII regions and the faint DIG.

Using diagnostic diagrams which compare the $[\text{OIII}]$, $[\text{NII}]$, and $[\text{SII}]$ emission to the brightest Balmer lines, we have shown how most of the emission features found in the DIG are consistent with even the simplest photoionization models. However, the $[\text{SII}]$ emission from the DIG cannot be explained by these simple models. The increase in $[\text{SII}]$ emission with decrease in $\text{H}\alpha$ surface brightness we have observed is well explained by the diluted radiation field photoionization models of Domgörgen & Mathis (1994). There is no evidence for shock ionization in the DIG layer of M31.

We would like to acknowledge the insightful discussions with Don Garnett on abundance gradient effects on emission-line ratios in spiral galaxies, and Stacy McGaugh on empirical abundance calibrators. We graciously thank Charles Hoopes for reading and commenting on the manuscript during its development. The comments from an anonymous referee helped to clarify presentation of the results. This work has been supported by NSF grant AST-9617014 and a Cottrell Scholar Award from Research Corporation to R.A.M.W.

8. Appendix : Special Cases

Of the 46 discrete HII regions observed we have identified 9 diffuse nebulae, 16 center-bright nebulae, 12 extended complexes, and 9 discrete ring structures. In a very few cases, the new classification used is in disagreement with the WB92 classification. The subapertures obtained for structures within extended nebulae have also been classified using the same nomenclature. It is important to note, in this case, that a morphological classification of “ring” can mean that the spectrum contains light across an entire object which appears as an $\text{H}\alpha$ ring or can mean that the spectrum is from a section of a ring; a distinction is made only in Fig 4 and Fig 5 where the point size indicates if the object is a discrete nebula or a substructure within a nebula.

We have also obtained spectra of large complexes and other nebulae within which are embedded SNR candidates from the BW93 catalog. Here we provide a set of brief descriptions for these objects as well as for objects which have been re-classified or which require a more detailed description of their morphology. The central positions for apertures

are labelled in the finding charts, Fig 1a and Fig 1b.

K87 was classified as a center-brightened source by WB92 although it consists of a bright compact source (K87.b) centered within a faint diffuse shell of emission approximately 150 pc in diameter. It is unclear whether this diffuse ring of gas is really associated with the bright knot, especially since the spectral properties are quite different. The line fluxes in the spectrum of the west filament (K87.a) are included in Table 4; the east filament had insufficient signal-to-noise to include in our results.

K103.a is a filamentary structure which appears on the far northern edge of a confirmed supernova remnant, K103A. Several spectra were extracted to study the complicated structures in the large complex, K103. The spectra of various knots and filaments do show the elevated [SII]/H α ratio indicating shock-ionization and confirm the nature of the embedded supernova remnant candidate. The filament K103.a, however, has a very low [SII] ratio, suggesting that it is actually not part of the supernova remnant.

K132 is listed as a diffuse nebula in WB92 but appears to be a bright compact source embedded within an amorphous diffuse nebula. This knot is a center-brightened 25 pc HII region. The diffuse gas surrounding this object is too faint to obtain a good spectrum.

K310 is one of two BW93 supernova remnant candidates we have rejected due to the low [SII]/H α ratio observed in its spectrum. It is a 55 pc, very diffuse and faint (E.M. \approx 90 pc cm $^{-6}$) amorphous nebula. Though it is fainter than our adopted DIG cutoff surface brightness, it is not classified as DIG because it appears as a discrete nebula.

K446 was also suspected to be a supernova remnant due to the high [SII]/H α ratio obtained from line images. Our spectroscopy has ruled out this candidate however, which shows a ratio of only 0.24. The low ratio determined from the images was affected by a few bad pixels.

K496 is a large HII region which contains an embedded SNR candidate, K496A (BW93). We did not obtain a spectrum of the candidate however. The section of the object for which we have obtained a spectrum does not show the signature enhanced [SII]/H α line ratio so we have included K496 with the HII regions.

K525 is a large HII region complex consisting of several diffuse structures, faint arcs, bright compact knots and includes an embedded supernova remnant candidate, K525A (BW93) toward the center of the region. All but the central aperture which corresponds to the supernova remnant (K525.c), show [SII]/H α ratios typically found in photoionized nebulae.

K526 The spectrum obtained for this HII region complex contains light from an embedded supernova remnant candidate K526A, and a center-bright nebula with a diameter near 80

pc. The [SII]/H α ratio in two spectra (K526.b and K526.c) are enhanced, confirming the embedded SNR; the other aperture, K526.a, which corresponds to the compact source, shows [SII] emission typical of HII regions.

K877 is a large ($d \approx 200$ pc) complex which contains an embedded Wolf-Rayet star (#1201 in MLA93) near the center of a small ring shaped structure.

K932 was classified as a single object in the WB92 catalog, though closer inspection of the H α image reveals that it is actually a cluster of several very bright compact sources and may include a small faint complete ring to the north. The first spectrum (K932.a) is that of a small knot near the rim of the faint ring-like HII region. The second (K932.b) is a bright compact source with a diameter of about 40 pc. We have listed K932 as a complex because it does not appear to be a discrete nebula.

REFERENCES

Aller, L. H. 1942, ApJ, 95, 52
Baldwin, J. A., Phillips, M. M., Terlevich, R. 1981, PASP, 93, 5
Binette, L., Dopita, M. A., Dodorico, S., Benvenuti, P. 1982, A&A, 115, 315
Blair, W. P., Kirshner, R. P., Chevalier, R.A. 1981, ApJ, 247, 879
Blair, W. P., Kirshner, R. P., Chevalier, R.A. 1982, ApJ, 254, 50
Blair, W. P., & Long, ,1997, ApJ Suppl., 108, 261
Braun, R. 1991, ApJ, 372, 54
Braun, R. & Walterbos, R. A. M. 1993, A&A Suppl., 98, 327
Burstein, D. & Heiles, C. 1984, ApJ Suppl., 54, 33
DeRobertis, M. M., Dufour, R. J., Hunt, R. W. 1987, RASC, 81, 195
Dennefeld, M. & Kunth, D. 1981, AJ, 86, 989
Domgörzen, H. & Mathis, J. S. 1994, ApJ, 428, 647
Dopita, M. A. 1977, A&A, 56, 303
Dopita, M. A., Binette, L., Dodorico, S., Benvenuti, P. 1984a, ApJ, 276, 653
Dopita, M. A. & Evans, I. M. 1986, ApJ, 307, 431
Dopita, M. A., Mathewson, D. S., Ford, V. L. 1977, ApJ, 214, 179
Edmunds, M. G. & Pagel, B. E. J. 1984, MNRAS, 211, 507

Evans, I. N. 1986, ApJ, 309, 544

Evans, I. N. & Dopita, M. A. 1985, ApJ Suppl., 58, 125

Ferguson, A. M. N., Wyse, R. F. G., Gallagher, J. S., III, Hunter, D. A. *et al.* 1996, AJ, 111, 2265

Freedman, W. L. & Madore, B. F. 1990, ApJ 365, 186

Garnett, D. R., Shields, G. A., Skillman, E. D., Sagan, S. P., Dufour, R. J. 1997, ApJ, 489, 63

Greenawalt, B., Walterbos, R. A. M., Braun, R. 1997, ApJ, 483, 666

Henry, R. B. C. & Howard, J. W. 1995, ApJ, 438, 170

Hoopes, C. G., Walterbos, R. A. M., Greenawalt, B. E. 1996, AJ, 112, 1429

Humphreys, R. M., Massey, P., Freedman, W. L. 1990, AJ, 99, 84

Kaler, J. B., Aller, L. H., Czyzak, S. J., Epps, H. W. 1976, ApJ Suppl., 31, 163

Kennicutt, R. C., Jr. 1984, ApJ, 287, 116

Kennicutt, R. C., Jr. & Garnett, D. R. 1996, ApJ, 456, 504

Kennicutt, R. C., Jr., Tamblyn, P., & Congdon, C. W. 1994, ApJ, 435, 22

Magnier, E. A., Prins, S., van Paradijs, J., Lewin, W. H. G., Supper, R., Hasinger, G., Pietsch, W., Truemper, J. 1995, A&A Suppl., 114, 215

Magnier, E. A., Primini, F. A., Prins, S., van Paradijs, J., Lewin, W. H. G. 1997, ApJ, 490, 649

Martin, C. L. 1997, ApJ, 491, 561

Meyssonnier, N., Lequeux, J., Azzopardi, M. 1993, A&AS, 102, 251

Osterbrock, D. E. 1989, *Astrophysics of Gaseous Nebulae and Active Galactic Nuclei* (Mill Valley, CA: University Science Books)

Pagel, B. E. J., Edmunds, M. G., Blackwell, D. E., Chun, M. S., Smith, G. 1979, MNRAS, 189, 95

Pagel, B. E. J., Edmunds, M. G., Smith, G. 1980, MNRAS, 193, 219

Pellet, A., Astier, N., Viale, G., Coutes, G., Maucherat, A., Monnet, G., Simien, F. 1978, A&AS, 31, 439

Rand, R. J., 1998, ApJ, 501, 137

Raymond, J. C. 1979, ApJ Suppl., 39, 1

Savage, B. D. & Mathis, J. S. 1979, ARA&A, 17, 73

Scowen, P. A., Dufour, R. J., Hester, J. J. 1992, AJ, 104, 92

Searle, L. 1971, ApJ, 168, 327

Shields, G. A. & Filippenko, A. V. 1990, AJ, 100, 1034

Shull, J. M. & McKee, C. F. 1979, ApJ, 227, 131

Szeifert, T., Humphreys, R. M., Davidson, K., Jones, T. J., Stahl, O., Wolf, B., Zickgraf, F. J. 1996, A&A, 314, 131

Vilchez, J. M. 1989, Ap&SS, 157, 61

Walterbos, R. A. M. 1988, in Galactic and Extragalactic Star Formation, R. E. Pudritz & M. Fich Eds. NATO ASI Series, Kluwer, 361

Walterbos, R. A. M. & Braun, R. 1992, A&A Suppl., 92, 625

Walterbos, R. A. M. & Braun, R. 1994, ApJ, 431, 156

Walterbos, R. A. M. & Schwering, P. B. W. 1987, A&A, 180, 27

Wang, J., Heckman, T. M., Lehnert, M. D. 1997, ApJ, 491, 114

Wilcots, E. M. 1992, AJ, 107, 1338

Zaritsky, D., Hill, J. M., Elston, R. 1990, AJ, 99, 1108

Zaritsky, D. 1992, ApJ, 390, 73

Table 1. Slit Positions

Spectrum	Slit Center		PA ^{1,2}	WB92 Field	Target Objects
	RA(2000)	DEC(2000)			
K59	0:43:01.0	41:38:28.5	156.9	15	K59, K87, K82, K91, K92
K86	0:43:00.0	41:36:54.5	135.4	15	K68, K70, K76, K78, K81, K86 ³
K103	0:43:21.0	41:44:05.4	129.6	14	K132, K145, K103 ^{3,5}
K230	0:43:56.0	41:12:46.3	238.0	3	K230 ³ K244, K250, K252 ³
K310	0:44:10.0	41:33:03.3	92.6	1	K310 ⁴ K314, K315, K316
K327	0:44:17.0	41:18:30.3	119.6	4	K330, K327 ⁴ K343, K353
K425	0:44:25.0	41:20:06.3	105.0	4	K391, K403, K425 ⁴
K434	0:44:34.1	41:51:48.2	180.9	12	K531, K496 ³ K480, K434, K442
K446	0:44:28.0	41:21:46.3	147.5	5	K414, K446 ³ K450
K506	0:44:39.0	41:25:32.2	185.0	6	K447, K461, K490 ³ K506 ³ K536 ⁶
K526	0:44:42.0	41:27:02.2	103.5	6	K525 ³ K526 ³ K527 ³ K536 ⁶
K594	0:44:59.1	41:55:21.2	195.4	11	K594 ⁴ K653 ⁵
K717	0:45:11.1	41:37:35.2	106.1	8	K703, K722, K717 ⁴
K856	0:45:37.1	41:55:06.1	207.5	10	K772, K787, K838, K851, K856 ³
K884	0:45:51.1	42:10:29.1	222.6	19	K884 ⁴ K877 ⁵
K934	0:46:34.2	42:12:03.0	265.0	18	K927, K931, K932, K934 ⁴

¹Slit position angles are listed in degrees.

²Exposure time for each slit position is 30 minutes.

³Object contains an embedded Braun & Walterbos (1993) SNR candidate.

⁴Object is listed as a Braun & Walterbos (1993) SNR candidate.

⁵Object contains a Wolf-Rayet star candidate.

⁶Object was observed at two position angles.

Table 2. HII Region Nebular Conditions

Object ¹	Aperture	R _g ² (kpc)	H α /H β ³	A _V ⁴ (mag)	R _[SII] ⁵	n _e (cm ⁻³)
K59 (HP600)		16.0	3.6(0.2)	0.7(0.2)	1.5(0.2)	<10
K68		16.1	4.3(0.2)	1.3(0.2)	1.7(0.3)	<10
K70 (HP576,581,587,592)		16.1	6.3(0.3)	2.4(0.2)	1.7(0.1)	<10
	a	16.1	7.0(0.4)	2.7(0.2)	1.6(0.1)	<10
	b	16.1	6.6(0.3)	2.5(0.2)	2.7(0.2)	<10
	c	16.1	6.4(0.3)	2.4(0.2)	1.3(0.1)	130
	d	16.1	5.9(0.3)	2.2(0.2)	1.6(0.1)	<10
	e	16.1	7.8(0.6)	3.0(0.2)	1.5(0.4)	<10
K76		11.7	9.0(0.5)	2.8(0.2)	1.4(0.2)	40
K78		11.7	6.6(0.4)	2.5(0.2)	1.6(0.2)	<10
K81		11.7	5.2(0.3)	1.8(0.2)	1.8(0.2)	<10
	a	11.7	5.0(0.3)	1.7(0.2)	2.1(0.3)	<10
	b	11.7	5.0(0.3)	1.7(0.2)	1.5(0.2)	<10
K82	a	16.0	4.1(0.2)	1.1(0.2)	1.5(0.2)	<10
	b	16.0	3.8(0.3)	0.9(0.2)	1.9(0.8)	<10
K87 (HP603,609)		16.0	4.8(0.2)	1.6(0.2)	1.5(0.2)	<10
	a	16.0	5.0(0.3)	1.7(0.2)	1.5(0.2)	<10
	b	16.0	5.7(0.3)	2.1(0.1)	1.5(0.1)	<10
K91 (HP613)		11.6	5.7(0.3)	2.1(0.2)	1.4(0.1)	40
K92 (HP612)		11.6	9.7(0.5)	3.7(0.1)	1.3(0.1)	130
K103 (HP679,680)	a	15.8	3.3(0.2)	0.4(0.2)	1.1(0.2)	380
K132		15.7	4.8(0.3)	1.6(0.2)	1.7(0.2)	<10
K145		11.5	3.6(0.2)	0.7(0.2)	1.0(0.3)	580
K244		12.0	6.7(0.4)	2.6(0.2)	0.9(0.2)	850
K250 (HP468)		12.1	4.5(0.2)	1.4(0.2)	1.4(0.1)	40
	a	12.1	4.2(0.2)	1.2(0.1)	1.3(0.1)	130
	b	12.1	4.8(0.3)	1.6(0.2)	1.4(0.2)	40
K310 [†]		5.4	3.9(0.3)	1.0(0.2)	1.0(0.3)	580
K314 (HP632)		5.4	4.0(0.2)	1.0(0.1)	1.4(0.1)	40
K315 (HP643,649)		5.4	3.5(0.2)	0.6(0.1)	1.3(0.1)	130
	a	5.4	4.3(0.2)	1.3(0.2)	1.0(0.1)	580
	b	5.4	3.9(0.2)	1.0(0.2)	1.1(0.2)	380
	c	5.4	3.7(0.2)	0.8(0.2)	1.3(0.1)	130
	d	5.4	3.5(0.2)	0.6(0.1)	1.4(0.1)	40
	e	5.4	3.1(0.2)	0.3(0.1)	1.3(0.1)	130
K330 (HP533)		9.0	4.0(0.2)	1.0(0.2)	1.5(0.1)	<10
K343		9.0	4.6(0.3)	1.5(0.2)	1.2(0.2)	240
K353		12.2	7.2(0.5)	2.8(0.2)	1.3(0.2)	130
	a	12.2	6.0(0.3)	2.2(0.2)	1.4(0.1)	40
	b	12.2	7.2(0.6)	2.8(0.2)	2.9(1.4)	<10
	c	12.2	5.7(0.5)	2.1(0.2)	0.9(0.3)	850
K391		9.0	4.9(0.4)	1.6(0.3)	0.9(0.1)	850

Table 2—Continued

Object ¹	Aperture	R _g ² (kpc)	H α /H β ³	A _V ⁴ (mag)	R _[SII] ⁵	n _e (cm ⁻³)
K403 (HP549,550,556)		9.0	3.6(0.2)	0.7(0.1)	1.4(0.1)	40
	a	9.0	3.9(0.2)	1.0(0.2)	1.1(0.1)	380
	b	9.0	3.9(0.2)	1.0(0.2)	1.4(0.2)	40
	c	9.0	4.3(0.2)	1.3(0.2)	1.3(0.2)	130
	d	9.0	3.8(0.2)	0.9(0.1)	1.3(0.1)	130
	e	9.0	3.3(0.2)	0.4(0.2)	1.3(0.1)	130
	f	9.0	3.6(0.2)	0.7(0.2)	1.4(0.2)	40
	g	9.0	3.4(0.2)	0.6(0.1)	1.4(0.1)	40
K414		9.0	3.6(0.2)	0.7(0.1)	1.3(0.1)	130
		9.1	3.9(0.3)	1.0(0.2)	1.7(0.2)	<10
	a	9.1	5.6(1.6)	2.1(0.9)	<4.3	<10
	b	9.1	3.5(0.3)	0.6(0.2)	1.8(0.4)	<10
K434		9.1	3.6(0.2)	0.7(0.2)	1.9(0.2)	<10
		10.9	7.3(0.4)	2.8(0.2)	1.5(0.4)	<10
K442 (HP782)		10.9	5.9(0.3)	2.2(0.2)	1.6(0.2)	<10
	a	10.9	6.3(0.4)	2.4(0.2)	1.4(0.2)	40
	b	10.9	6.4(0.4)	2.4(0.2)	1.6(0.2)	<10
	c	10.9	4.3(0.2)	1.3(0.2)	1.7(0.2)	<10
	d	10.9	4.3(0.3)	1.3(0.2)	1.6(0.2)	<10
K446 [†]		9.1	4.1(0.2)	1.1(0.2)	1.2(0.1)	240
K447		9.1	4.1(0.2)	1.1(0.2)	2.1(0.3)	<10
K450	a	12.3	12.3(3.1)	4.4(0.8)	1.3(0.4)	130
	b	12.3	3.3(0.2)	0.5(0.2)	0.9(0.1)	850
K461		9.3	3.6(0.2)	0.7(0.2)	1.6(0.1)	<10
K480		10.9	7.1(1.3)	2.7(0.3)	1.5(0.4)	<10
K496 (HP778)		10.9	5.4(0.3)	1.9(0.1)	1.3(0.1)	130
K525 (HP625,629)		9.2	3.7(0.2)	0.8(0.1)	1.5(0.1)	<10
	a	9.2	3.4(0.2)	0.5(0.2)	1.5(0.2)	<10
	b	9.2	4.3(0.2)	1.3(0.2)	1.1(0.1)	380
	d	9.2	3.2(0.2)	0.3(0.2)	0.8(0.4)	1500
	e	9.2	3.3(0.2)	0.4(0.2)	2.2(0.4)	<10
K526		9.2	4.7(0.3)	1.5(0.2)	1.3(0.1)	130
	a	9.2	4.0(0.2)	1.0(0.2)	1.4(0.1)	40
K531		10.8	6.1(0.3)	2.3(0.2)	1.2(0.1)	240
K536 (HP622)		9.2	3.1(0.2)	0.3(0.2)	2.5(1.2)	<10
	a	9.2	2.8(0.2)	0.0(0.0)	1.2(0.1)	240
	b	9.2	3.3(0.2)	0.4(0.2)	1.7(0.6)	<10
K536 ⁶		12.3	2.9(0.2)	0.04(0.2)	3.9(1.9)	<10
K703 (HP721,722)		9.6	3.0(0.2)	0.1(0.2)	1.3(0.1)	130
	a	9.6	4.1(0.3)	1.1(0.2)	1.3(0.2)	130
	b	9.6	8.6(0.7)	3.3(0.2)	1.6(0.3)	<10
	c	9.6	4.2(0.3)	1.2(0.2)	1.3(0.2)	130
	d	9.6	3.8(0.2)	0.9(0.2)	1.3(0.2)	130
	e	9.6	3.1(0.2)	0.3(0.1)	1.4(0.1)	40
	f	9.6	4.8(0.2)	1.6(0.1)	1.4(0.1)	40

Table 2—Continued

Object ¹	Aperture	R _g ² (kpc)	H α /H β ³	A _V ⁴ (mag)	R _[SII] ⁵	n _e (cm ⁻³)
K722 (HP720,857)		9.6	4.5(0.3)	1.4(0.2)	1.2(0.2)	240
	a	9.6	4.4(0.3)	1.3(0.2)	1.4(0.2)	40
	b	9.6	5.1(0.4)	1.7(0.2)	1.3(0.2)	130
K772		10.1	5.4(0.4)	1.9(0.2)	2.3(0.1)	<10
K787 (HP857)		10.1	6.7(0.6)	2.6(0.3)	1.7(0.3)	<10
K838		10.3	7.0(0.4)	2.7(0.2)	1.2(0.2)	240
K851		10.4	3.8(0.2)	0.9(0.1)	1.4(0.1)	40
K856 (HP879)	a	10.4	4.6(0.3)	1.5(0.2)	1.7(0.2)	<10
	b	10.4	4.4(0.2)	1.3(0.2)	1.4(0.1)	40
	d	10.4	4.5(0.2)	1.4(0.2)	1.4(0.1)	40
K877 (HP930,931,933)		14.4	3.8(0.2)	0.9(0.2)	0.9(0.2)	850
	a	14.4	3.6(0.3)	0.7(0.2)	1.3(0.3)	130
	b	14.4	4.0(0.2)	1.0(0.2)	1.1(0.1)	380
	c	14.4	4.5(0.4)	1.4(0.3)	0.8(0.2)	1500
	d	14.4	3.0(0.2)	0.1(0.2)	0.9(0.2)	850
	e	14.4	3.6(0.2)	0.7(0.2)	0.9(0.2)	850
K927 (HP962,964)		14.2	3.8(0.2)	0.9(0.2)	1.2(0.1)	240
	a	14.2	3.8(0.2)	0.9(0.2)	1.3(0.1)	130
	b	14.2	3.7(0.2)	06.8(0.2)	1.2(0.1)	240
K931 (HP970)		14.2	4.9(0.2)	1.6(0.2)	1.3(0.1)	130
K932 (HP968)		14.1	4.1(0.2)	1.1(0.1)	1.3(0.1)	130
	a	14.1	4.2(0.2)	1.2(0.1)	1.4(0.1)	40
	b	14.1	4.0(0.2)	1.0(0.1)	1.3(0.1)	130

¹Cross-references listed for objects in Pellet *et al.* (1978); complexes may be consistent with more than one HP object.

²Radial distances taken from Walterbos & Braun (1992).

³Ratio based on observed H α and H β fluxes.

⁴Extinction determined using A(V) = 3.1E(B-V) and H α /H β _{int}=2.86.

⁵R_[SII]=6716Å/6731Å

⁶Spectrum of K536 obtained with second position angle pointing.

[†]Spectroscopically rejected SNR candidate.

Table 3. SNR Nebular Conditions

Object ¹	Aperture	R _g ² (kpc)	H α /H β ³	A _V ⁴ (mag)	R _[SII] ⁵	n _e (cm ⁻³)
K86		11.7	3.4(0.2)	0.4(0.2)	1.4(0.1)	40
	a	11.7	3.4(0.2)	0.4(0.2)	1.3(0.1)	130
	b	11.7	3.1(0.2)	0.1(0.2)	1.4(0.1)	40
K103A	b	15.8	4.0(0.2)	0.9(0.1)	1.4(0.1)	40
	c	15.8	3.7(0.2)	0.6(0.1)	1.3(0.1)	130
	d	15.8	4.4(0.2)	1.1(0.2)	1.4(0.1)	40
	e	15.8	4.1(0.3)	0.9(0.2)	1.7(0.4)	<10
		12.0	3.4(0.2)	0.4(0.2)	1.2(0.1)	240
K230A	a	12.0	3.8(0.3)	0.7(0.2)	1.2(0.1)	240
	b	12.0	4.0(0.3)	0.9(0.2)	1.5(0.2)	<10
		8.7	3.6(0.2)	0.5(0.1)	1.3(0.1)	130
K252 (BA22)	a	8.7	3.3(0.2)	0.3(0.1)	1.3(0.1)	130
	b	8.7	4.0(0.2)	0.9(0.1)	1.3(0.1)	130
		12.2	4.8(0.2)	1.4(0.1)	1.1(0.1)	380
K327		12.2	3.5(0.2)	0.4(0.2)	1.9(0.2)	<10
	a	12.2	3.4(0.3)	0.4(0.3)	2.1(0.4)	<10
	b	12.2	4.0(0.3)	0.9(0.2)	1.6(0.2)	<10
K425		9.2	3.6(0.2)	0.5(0.2)	1.6(0.1)	<10
	a	9.2	3.5(0.2)	0.4(0.2)	1.4(0.1)	40
	b	9.2	3.1(0.2)	0.1(0.2)	1.6(0.2)	<10
	c	9.2	3.6(0.2)	0.5(0.2)	1.6(0.1)	<10
		9.2	5.9(0.4)	1.6(0.2)	1.4(0.1)	40
K490A	c	9.2	3.8(0.2)	0.7(0.1)	1.4(0.1)	40
	a	9.2	3.1(0.2)	0.1(0.2)	1.6(0.2)	<10
K506A	b	9.2	5.1(0.3)	1.6(0.2)	1.4(0.2)	40
	c	9.2	8.9(0.9)	3.3(0.3)	0.9(0.2)	850
		9.2	4.1(0.2)	1.0(0.2)	1.7(0.2)	<10
	a	10.7	7.8(0.4)	2.9(0.2)	1.4(0.1)	40
		9.6	5.9(0.4)	1.6(0.2)	1.0(0.1)	580
K525A (BA100)	c	10.4	4.3(0.2)	1.1(0.1)	1.5(0.1)	<10
		14.4	4.2(0.2)	1.0(0.2)	1.4(0.1)	40
K526A	a	14.4	3.7(0.2)	0.6(0.1)	1.5(0.1)	<10
	b	14.4	5.0(0.4)	1.5(0.2)	1.2(0.2)	240
		14.4	3.9(0.2)	0.8(0.2)	1.5(0.1)	<10
K527A		14.4	3.9(0.2)	0.8(0.2)	1.5(0.1)	<10
		10.7	7.8(0.4)	2.9(0.2)	1.4(0.1)	40
K594		9.6	5.9(0.4)	1.6(0.2)	1.0(0.1)	580
		10.4	4.3(0.2)	1.1(0.1)	1.5(0.1)	<10
K717 (BA160)	c	14.4	4.2(0.2)	1.0(0.2)	1.4(0.1)	40
		14.4	3.7(0.2)	0.6(0.1)	1.5(0.1)	<10
K856A (BA212)	a	14.4	5.0(0.4)	1.5(0.2)	1.2(0.2)	240
	b	14.4	3.9(0.2)	0.8(0.2)	1.5(0.1)	<10
		14.4	3.9(0.2)	0.8(0.2)	1.5(0.1)	<10
K884 (BA650)	a	14.4	3.7(0.2)	0.6(0.1)	1.5(0.1)	<10
	b	14.4	5.0(0.4)	1.5(0.2)	1.2(0.2)	240
K934		14.4	3.9(0.2)	0.8(0.2)	1.5(0.1)	<10

¹Cross-references are listed for SNRs in Blair, Kirshner & Chevalier (1981) and Blair, Kirshner & Chevalier (1982).

²Radial distances taken from Walterbos & Braun (1992).

³Ratio based on observed H α and H β fluxes.

⁴Extinction determined using A(V) = 3.1E(B-V) and H α /H β_{int} =3.00.

⁵R_[SII]=6716Å/6731Å

Table 4. HII Region Nebular Line Ratios

Object ¹	Aperture	W _{ap} ('')	E.M. H α	Reddening Corrected Line Ratios ²				Morphology ³
				[OII]/H β	[OIII]/H β	[NII]/H α	[SII]/H α	
K59 (HP600)		26.9	109	2.0(0.2)	< 0.1	0.24(0.02)	0.22(0.02)	diffuse
K68		5.5	311	1.4(0.2)	2.1(0.1)	0.54(0.03)	0.14(0.01)	center-bright
K70 (HP576,581,586,587,592)		55.9	920	1.9(0.2)	0.40(0.02)	0.41(0.02)	0.32(0.02)	complex
	a	7.6	1097	1.3(0.3)	0.30(0.01)	0.39(0.02)	0.33(0.02)	diffuse
	b	9.0	1557	1.3(0.2)	0.47(0.02)	0.38(0.02)	0.37(0.02)	diffuse
	c	9.0	1120	2.6(0.3)	0.29(0.01)	0.46(0.03)	0.28(0.02)	center-bright
	d	10.4	1089	1.6(0.2)	0.40(0.02)	0.35(0.02)	0.25(0.01)	ring
	e	3.5	710	< 3.9	< 0.7	0.46(0.05)	0.28(0.04)	diffuse
K76		8.3	1095	< 4.3	< 0.5	0.33(0.03)	0.32(0.02)	center-bright
K78		8.3	651	< 1.9	< 0.3	0.36(0.03)	0.30(0.02)	center-bright
K81		15.9	262	1.7(0.3)	< 0.2	0.34(0.03)	0.35(0.02)	ring
	a	3.5	263	< 1.2	< 0.3	0.37(0.04)	0.38(0.03)	ring
	b	6.9	227	2.1(0.4)	< 0.3	0.40(0.04)	0.38(0.03)	ring
K82	a	11.0	213	1.7(0.2)	< 0.3	0.45(0.04)	0.35(0.03)	ring
	b	6.9	85	< 1.0	0.44(0.03)	0.17(0.04)	0.17(0.04)	ring
K87 (HP603,609)		52.4	561	2.3(0.2)	2.5(0.1)	0.45(0.02)	0.27(0.02)	center-bright+ring
	a	11.0	488	2.0(0.2)	0.52(0.02)	0.38(0.03)	0.32(0.02)	ring
	b	15.2	1936	3.4(0.2)	3.9(0.1)	0.44(0.02)	0.25(0.01)	center-bright
K91 (HP613)		9.7	862	2.5(0.2)	0.31(0.03)	0.46(0.02)	0.34(0.02)	ring
K92 (HP612)		10.4	4970	2.7(0.3)	0.57(0.02)	0.47(0.02)	0.21(0.01)	center-bright
K103 (HP679,680)	a	7.6	103	3.7(0.5)	0.80(0.04)	0.51(0.05)	0.35(0.04)	diffuse
K132		13.8	444	2.8(0.3)	2.4(0.1)	0.53(0.03)	0.27(0.02)	center-bright
K145		7.5	152	0.7(0.2)	0.22(0.01)	0.47(0.05)	0.22(0.03)	center-bright
K244		9.0	519	< 2.8	< 0.5	0.38(0.03)	0.31(0.03)	diffuse
K250 (HP468)		19.3	723	4.7(0.3)	1.39(0.05)	0.51(0.03)	0.38(0.02)	ring
	a	19.3	347	7.5(0.4)	3.0(0.1)	0.73(0.03)	0.65(0.03)	ring
	b	29.7	241	2.7(0.3)	0.38(0.02)	0.39(0.02)	0.25(0.02)	ring
K310 [†]		13.8	91	2.1(0.3)	0.82(0.05)	0.56(0.06)	0.25(0.04)	diffuse
K314 (HP632)		17.3	1250	1.6(0.1)	0.13(0.01)	0.46(0.02)	0.29(0.01)	center-bright
K315 (HP643,649)		69.7	341	2.1(0.1)	0.37(0.01)	0.54(0.03)	0.22(0.01)	complex
	a	7.6	284	1.4(0.2)	< 0.3	0.51(0.03)	0.34(0.03)	diffuse
	b	4.8	193	1.4(0.2)	0.3(0.1)	0.46(0.04)	0.33(0.03)	diffuse
	c	12.4	572	1.2(0.1)	0.23(0.01)	0.45(0.02)	0.18(0.01)	diffuse
	d	9.0	546	2.7(0.1)	0.38(0.01)	0.64(0.03)	0.27(0.01)	ring
	e	6.9	288	3.6(0.2)	0.71(0.02)	0.73(0.04)	0.25(0.01)	ring
K330 (HP533)		19.3	178	4.6(0.3)	1.40(0.05)	0.76(0.05)	0.52(0.03)	diffuse
K343		14.5	115	3.9(0.5)	< 0.5	0.5(0.1)	0.56(0.05)	diffuse
K353		59.3	372	< 2.7	1.6(0.1)	0.17(0.02)	0.30(0.02)	complex
	a	13.1	561	2.1(0.5)	0.95(0.04)	0.35(0.02)	0.31(0.02)	ring
	b	4.1	438	< 4.9	0.84(0.05)	0.34(0.05)	0.20(0.04)	ring
	c	6.9	227	< 7.0	2.0(0.1)	0.17(0.04)	0.29(0.05)	center-bright
K391		5.5	133	5.3(0.7)	< 1.0	0.6(0.1)	< 0.4	center-bright

Table 4—Continued

Object ¹	Aperture	W _{ap} ('')	E.M. H α	Reddening Corrected Line Ratios ²				Morphology ³	
				[OII]/H β	[OIII]/H β	[NII]/H α	[SII]/H α		
K403 (HP549,550,556)		73	468.9	1.8(0.1)	0.25(0.01)	0.43(0.02)	0.28(0.01)	complex	
	a	4.8	233	1.6(0.2)	< 0.2	0.51(0.04)	0.33(0.02)	ring	
	b	5.5	271	1.3(0.2)	< 0.2	0.46(0.03)	0.37(0.02)	ring	
	c	9.0	355	1.4(0.1)	< 0.2	0.41(0.02)	0.30(0.02)	ring	
	d	9.7	482	1.6(0.1)	0.12(0.01)	0.47(0.02)	0.33(0.02)	center-bright	
	e	9.0	300	1.7(0.1)	0.26(0.01)	0.32(0.02)	0.28(0.01)	diffuse	
	f	7.6	387	1.8(0.1)	0.66(0.02)	0.41(0.02)	0.23(0.01)	diffuse	
	g	11.0	1198	1.8(0.1)	0.25(0.01)	0.45(0.02)	0.27(0.01)	center-bright	
K414		7.6	516	2.0(0.1)	0.26(0.01)	0.44(0.02)	0.27(0.01)	center-bright	
		49.0	115	2.9(0.3)	< 0.3	0.42(0.04)	0.40(0.03)	complex	
	a	17.3	124	3.7(1.5)	< 1.0	0.4(0.1)	0.2(0.1)	diffuse	
	b	22.8	53	2.0(0.2)	< 0.2	0.43(0.05)	0.39(0.05)	diffuse	
K434		c	15.9	154	2.8(0.2)	0.2(0.1)	0.22(0.02)	0.40(0.03)	ring
			11.0	1886	3.0(0.5)	0.91(0.04)	0.33(0.03)	0.12(0.01)	center-bright
K442 (HP782)			81.4	572	1.6(0.2)	0.37(0.02)	0.39(0.03)	0.29(0.02)	complex
	a		9.7	710	1.4(0.3)	1.2(0.1)	0.41(0.03)	0.27(0.02)	ring
	b		10.4	710	1.7(0.3)	< 0.3	0.37(0.03)	0.33(0.02)	ring
	c		9.0	262	2.0(0.2)	< 0.2	0.42(0.03)	0.38(0.03)	diffuse
K446 [†]		d	19.3	203	1.2(0.2)	0.59(0.03)	0.46(0.04)	0.39(0.03)	diffuse
			5.5	577	4.0(0.2)	0.48(0.02)	0.52(0.03)	0.24(0.02)	center-bright
K447			12.4	176	4.6(0.4)	3.3(0.1)	0.89(0.05)	0.43(0.03)	diffuse
K450	a		4.1	1775	47.4(4.5)	3.0(0.6)	0.47(0.05)	0.26(0.04)	ring
	b		15.9	77	1.8(0.2)	5.1(0.2)	0.52(0.05)	< 0.3	ring
K461			9.0	464	1.0(0.1)	< 0.05	0.52(0.03)	0.29(0.02)	diffuse
K480			4.8	456	3.6(1.1)	1.01(0.04)	0.5(0.1)	0.35(0.05)	ring
K496 (HP778)			15.9	1312	1.4(0.1)	< 0.08	0.40(0.02)	0.19(0.01)	center-bright
K525 (HP625,629)			50.4	535	2.5(0.1)	0.61(0.03)	0.47(0.04)	0.38(0.02)	complex
	a		4.2	189	1.3(0.1)	0.34(0.02)	0.47(0.04)	0.28(0.02)	ring
	b		4.8	436	1.7(0.2)	0.24(0.02)	0.36(0.03)	0.26(0.02)	ring
	d		4.8	112	1.0(0.2)	0.72(0.04)	0.47(0.05)	0.11(0.05)	diffuse
	e		8.3	175	1.7(0.1)	0.61(0.03)	0.52(0.04)	0.24(0.02)	diffuse
K526			53.1	424	1.0(0.2)	0.19(0.04)	0.43(0.03)	0.37(0.02)	complex
	a		24.8	473	1.2(0.1)	0.11(0.01)	0.38(0.02)	0.27(0.02)	center-bright
K531			2.7	1065	< 1.1	0.39(0.02)	< 0.1	< 0.1	center-bright
K536 (HP622)			11.0	75	1.4(0.2)	< 0.4	0.46(0.04)	0.18(0.03)	ring
	a		4.1	44	1.3(0.2)	< 0.6	0.24(0.05)	< 0.4	ring
	b		6.9	92	1.6(0.2)	< 0.4	0.45(0.04)	0.22(0.03)	ring
K536 ⁴			11.0	51	1.0(0.2)	< 0.3	0.31(0.04)	0.25(0.04)	ring
K703 (HP721,722)			102.1	134	1.8(0.1)	1.35(0.05)	0.32(0.02)	0.35(0.02)	complex
	a		10.4	109	2.2(0.3)	< 0.4	0.6(0.1)	0.49(0.05)	ring
	b		28.3	520	10.4(1.6)	1.1(0.1)	0.6(0.1)	0.33(0.04)	ring
	c		12.4	197	1.8(0.3)	0.76(0.03)	0.48(0.04)	0.36(0.03)	diffuse
	d		7.6	197	2.4(0.2)	0.67(0.03)	0.49(0.04)	0.42(0.03)	diffuse
	e		9.0	492	2.7(0.2)	0.91(0.03)	0.39(0.02)	0.19(0.01)	center-bright
	f		13.8	2308	1.8(0.1)	1.63(0.05)	0.34(0.01)	0.17(0.01)	center-bright

Fig. 1a.— Slit positions and object aperture centers for all discrete objects and substructures in the 2D spectra. Grey-scale saturation levels in emission measure (pc cm⁻⁶) are given at the lower right hand corner of each image; image scaling is linear to bring out variations most dramatically. Images are 78" by 78". Complete images have been published in Walterbos & Braun (1992).

Table 4—Continued

Object ¹	Aperture	W _{ap} (")	E.M. H α	Reddening Corrected Line Ratios ²				Morphology ³
				[OII]/H β	[OIII]/H β	[NII]/H α	[SII]/H α	
K722 (HP720,857)		37	151.2	1.8(0.3)	0.36(0.02)	0.39(0.05)	0.35(0.04)	diffuse
	a	20.7	142	1.5(0.4)	0.51(0.03)	0.44(0.05)	0.41(0.04)	diffuse
	b	16.6	251	2.0(0.4)	0.46(0.02)	0.4(0.1)	0.43(0.04)	diffuse
K772		13.1	206	6.6(1.0)	< 0.7	0.8(0.1)	< 0.3	diffuse
K787 (HP857)		4.1	450	< 3.5	< 1.0	0.5(0.1)	0.7(0.1)	ring
K838		6.2	1183	2.2(0.6)	0.28(0.02)	0.51(0.04)	0.27(0.02)	center-bright
K851		8.3	1035	3.0(0.2)	0.45(0.02)	0.47(0.02)	0.24(0.01)	center-bright
K856 (HP879)	a	4.8	289	1.5(0.2)	< 0.23	0.46(0.04)	0.44(0.04)	ring
	b	6.9	639	3.8(0.2)	0.31(0.01)	0.48(0.03)	0.44(0.02)	center-bright
	d	7.6	581	3.0(0.2)	0.13(0.01)	0.42(0.03)	0.40(0.02)	ring
K877 (HP930,931,933)		77	127.9	4.7(0.4)	1.7(0.1)	0.48(0.05)	0.30(0.03)	complex
	a	5.5	93	2.7(0.5)	0.52(0.03)	0.6(0.1)	0.35(0.05)	diffuse
	b	20.0	269	5.0(0.3)	2.6(0.1)	0.40(0.03)	0.23(0.02)	ring
	c	4.8	137	5.8(0.7)	2.0(0.1)	0.5(0.1)	0.38(0.05)	ring
	d	5.5	62	3.9(0.4)	0.88(0.04)	0.7(0.1)	0.43(0.05)	diffuse
	e	9.7	134	5.4(0.4)	0.73(0.03)	0.54(0.05)	0.30(0.03)	diffuse
K927 (HP962,964)		26.9	200	3.2(0.2)	0.46(0.02)	0.42(0.03)	0.47(0.03)	ring
	a	9.7	304	2.5(0.2)	0.14(0.02)	0.41(0.02)	0.42(0.02)	ring
	b	5.5	1420	4.0(0.3)	0.44(0.02)	0.44(0.04)	0.54(0.03)	ring
K931 (HP970)		14.5	592	2.6(0.2)	0.24(0.01)	0.42(0.02)	0.24(0.01)	center-bright
K932 (HP968)		38.6	6973	1.9(0.1)	3.2(0.1)	0.21(0.01)	0.09(0.01)	complex
	a	18.6	3287	2.6(0.1)	1.8(0.1)	0.26(0.01)	0.10(0.01)	center-bright
	b	20.0	10283	1.7(0.1)	3.6(0.1)	0.20(0.01)	0.08(0.01)	center-bright

¹Cross-references listed for objects in Pellet *et al.* (1978); complexes may be consistent with more than one HP object.

²Upper limits are quoted as 3 σ .

³Morphological classification based on Walterbos & Braun (1992).

⁴Spectrum of K536 obtained with second position angle pointing.

†Spectroscopically rejected SNR candidate.

Table 5. HII Region Line Ratios for Rare Lines

Object ¹	Aperture	Reddening Corrected Line Ratios Relative to H β				
		[NeIII] 3868	HeI 4026	HeI 4471	HeI 5876	HeI 6678
K068		0.7(0.1)
K087 (HP603,609)		0.3(0.1)
	b	0.4(0.1)
K250 (HP468)		0.7(0.1)
	a	0.8(0.1)
K315 (HP643,649)	d	0.06(0.01)
K531		0.38(0.02)	...
K932 (HP968)		0.14(0.01)	...	0.04(0.01)	0.1(0.01)	0.03(0.01)
	a	0.1(0.1)	...	0.04(0.01)	0.1(0.01)	0.03(0.01)
	b	0.2(0.1)	0.02(0.01)	0.04(0.01)	0.1(0.01)	0.03(0.01)

¹Cross-references listed for objects in Pellet *et al.* (1978); complexes may be consistent with more than one HP object.

Fig. 1b.— Slit positions and object aperture centers for all discrete objects and substructures in the 2D spectra. Grey-scale saturation levels in emission measure (pc cm $^{-6}$) are given at the lower right hand corner of each image; image scaling is linear to bring out variations most dramatically. Images are 78" by 78". Complete images have been published in Walterbos & Braun (1992).

Table 6. Confirmed SNR Nebular Line Ratios

Object ¹	Aperture	W _{ap} ('')	E.M. H α	Reddening Corrected Line Ratios ²				
				[OII]/H β	[OIII]/H β	[OI]/H α	[NII]/H α	[SII]/H α
K86		24.2	193	6.5(0.3)	0.82(0.04)	0.13(0.01)	0.53(0.03)	0.60(0.03)
	a	15.9	216	6.1(0.3)	1.0(0.1)	0.13(0.01)	0.55(0.03)	0.60(0.03)
	b	4.1	142	5.9(0.3)	0.66(0.04)	0.15(0.01)	0.52(0.04)	0.67(0.04)
K103A	b	7.6	968	3.6(0.2)	1.2(0.1)	<0.06	0.53(0.02)	0.49(0.02)
	c	4.1	769	8.2(0.4)	1.5(0.1)	0.13(0.01)	0.77(0.03)	0.85(0.04)
	d	15.9	476	5.1(0.4)	1.1(0.1)	0.07(0.01)	0.59(0.03)	0.56(0.03)
	e	4.8	91	8.4(0.9)	0.7(0.1)	<0.2	0.69(0.06)	0.5(0.1)
		15.2	118	8.9(0.5)	3.4(0.2)	0.07(0.01)	0.75(0.05)	0.8(0.1)
K230A	a	8.3	186	9.6(0.8)	3.4(0.2)	0.09(0.01)	0.73(0.04)	0.67(0.04)
	b	5.5	138	12.7(0.8)	4.4(0.2)	0.15(0.05)	0.78(0.06)	0.8(0.1)
		8.9	683	9.5(0.4)	2.4(0.1)	0.21(0.01)	1.07(0.05)	1.1(0.1)
K252 (BA22)	a	4.8	467	9.5(0.4)	2.7(0.1)	0.25(0.01)	1.12(0.05)	1.13(0.05)
	b	4.1	1006	10.7(0.5)	2.4(0.1)	0.18(0.01)	1.04(0.05)	1.05(0.04)
		7.6	1065	6.7(0.4)	1.6(0.1)	0.25(0.01)	1.2(0.1)	1.02(0.04)
K327		9.7	58	9.3(0.7)	0.83(0.05)	0.22(0.04)	0.81(0.07)	0.9(0.1)
	a	4.1	37	9.9(1.0)	<0.74	0.5(0.1)	0.7(0.1)	1.0(0.1)
	b	4.1	95	10.5(0.8)	1.0(0.1)	<0.2	0.80(0.07)	1.0(0.1)
K490A		42.1	308	5.2(0.3)	0.76(0.04)	0.10(0.05)	0.75(0.04)	0.68(0.04)
	a	15.2	291	6.8(0.4)	0.97(0.05)	<0.25	0.90(0.05)	1.05(0.05)
	b	6.9	241	4.5(0.3)	0.87(0.04)	<0.19	0.63(0.03)	0.45(0.03)
K506A	c	9.7	431	3.6(0.2)	0.31(0.02)	<0.06	0.62(0.03)	0.54(0.03)
		7.6	452	3.5(0.4)	1.5(0.1)	<0.07	0.58(0.03)	0.62(0.05)
		20.0	1090	2.9(0.1)	0.66(0.03)	0.03(0.01)	0.5(0.02)	0.45(0.02)
K525A (BA100)	b	8.3	325	2.7(0.3)	0.52(0.10)	<0.16	0.55(0.04)	0.76(0.05)
	c	3.5	646	<2.7	<1.1	<0.43	0.29(0.05)	0.6(0.1)
		23.5	33	2.3(0.2)	0.29(0.02)	0.23(0.02)	0.48(0.03)	0.42(0.03)
K526A		8.3	2189	8.4(0.6)	0.9(0.1)	0.29(0.01)	1.07(0.05)	1.16(0.05)
	a	11.7	1107	6.2(0.4)	4.0(0.2)	0.19(0.01)	0.95(0.05)	0.88(0.04)
	b	6.9	675	4.8(0.3)	0.12(0.01)	0.08(0.01)	0.54(0.03)	0.68(0.03)
K527A		34.5	220	6.3(0.4)	0.09(0.03)	0.10(0.01)	0.48(0.03)	0.53(0.03)
	a	6.2	434	4.7(0.3)	0.15(0.01)	<0.06	0.50(0.03)	0.45(0.02)
	b	3.5	213	9.3(0.9)	0.6(0.1)	<0.36	0.50(0.06)	0.7(0.1)
K934		17.9	191	5.0(0.3)	0.41(0.02)	0.10(0.01)	0.52(0.03)	0.60(0.03)

¹Cross-references are listed for SNRs in Blair, Kirshner & Chevalier (1981) and Blair, Kirshner & Chevalier (1982).

²Upper limits are quoted as 3 σ .

Table 7. SNR [OIII] Temperatures

Object ¹	Aperture	$\frac{I(4959+5007)}{I(4363)}$	T _e (K) ²
K086	a	12.4(3.0)	58,500(15,000)
K230A		16.9(1.0)	39,000(3,400)
	a	12.9(0.7)	55,700(4,000)
K252 (BA22)		18.0(0.9)	37,000(3,000)
	a	17.5(0.9)	38,000(2,000)
	b	18.0(0.9)	37,000(3,000)

¹Cross-references are listed for SNRs in Blair, Kirshner & Chevalier (1981) and Blair, Kirshner & Chevalier (1982).

²Based on Kaler *et al.* (1976) formalism.

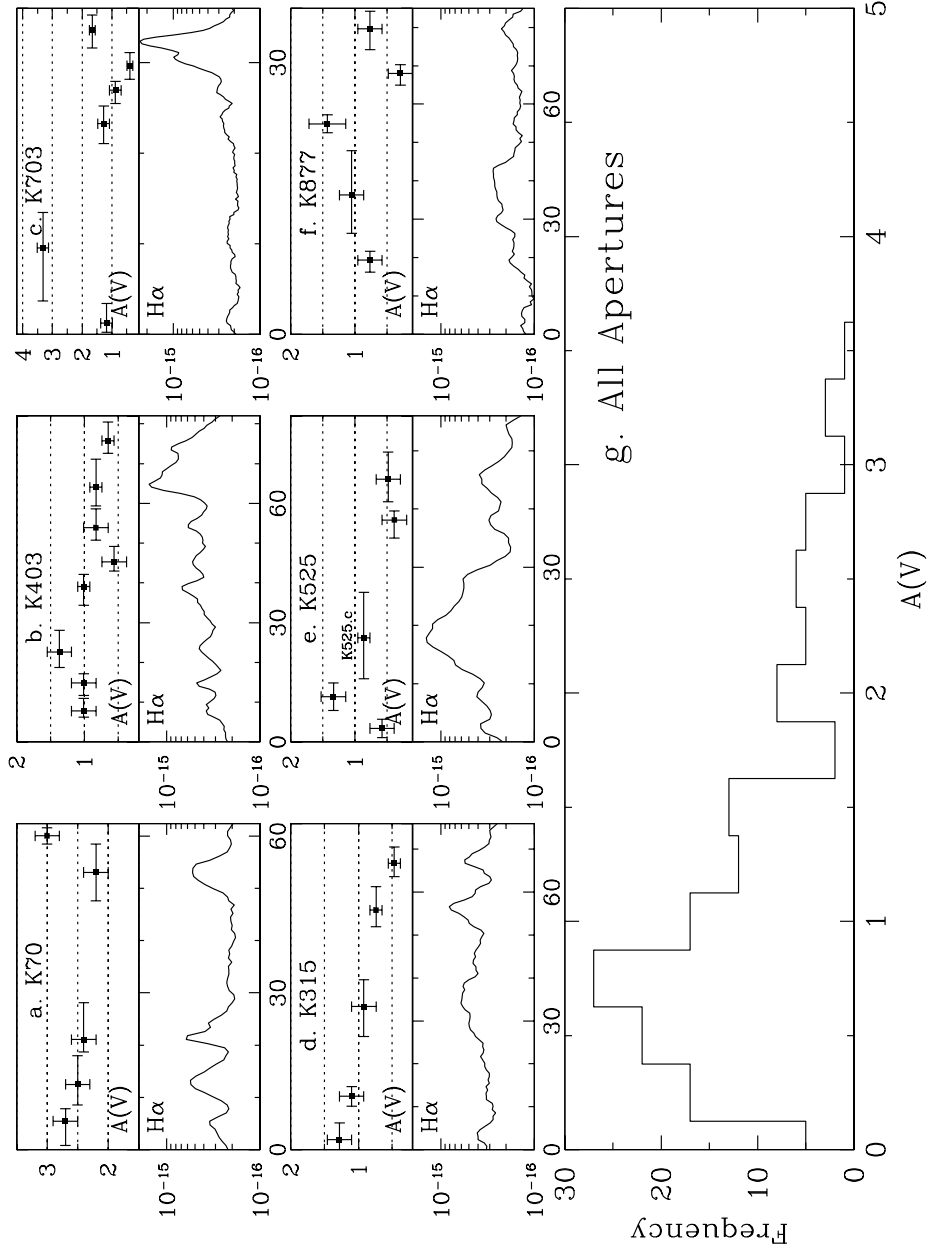


Fig. 2.— Extinction properties derived from the Balmer decrements of our complete sample of M31 nebulae. The separate panels in (a-f) show the variation of $A(V)$ (in magnitudes) across the spatial dimension (in arcseconds) of large HII region complexes along with the $H\alpha$ profile along the spectrum slit. Each point corresponds to a separate aperture and the bar delineates the section of the spectrum included in each aperture. An embedded SNR candidate in the HII region complex, K525, is identified. Dashed lines delineate the horizontal scale and are drawn only as a reference. Panel (g) shows the distribution of extinctions found in all the HII region and SNR spectra.

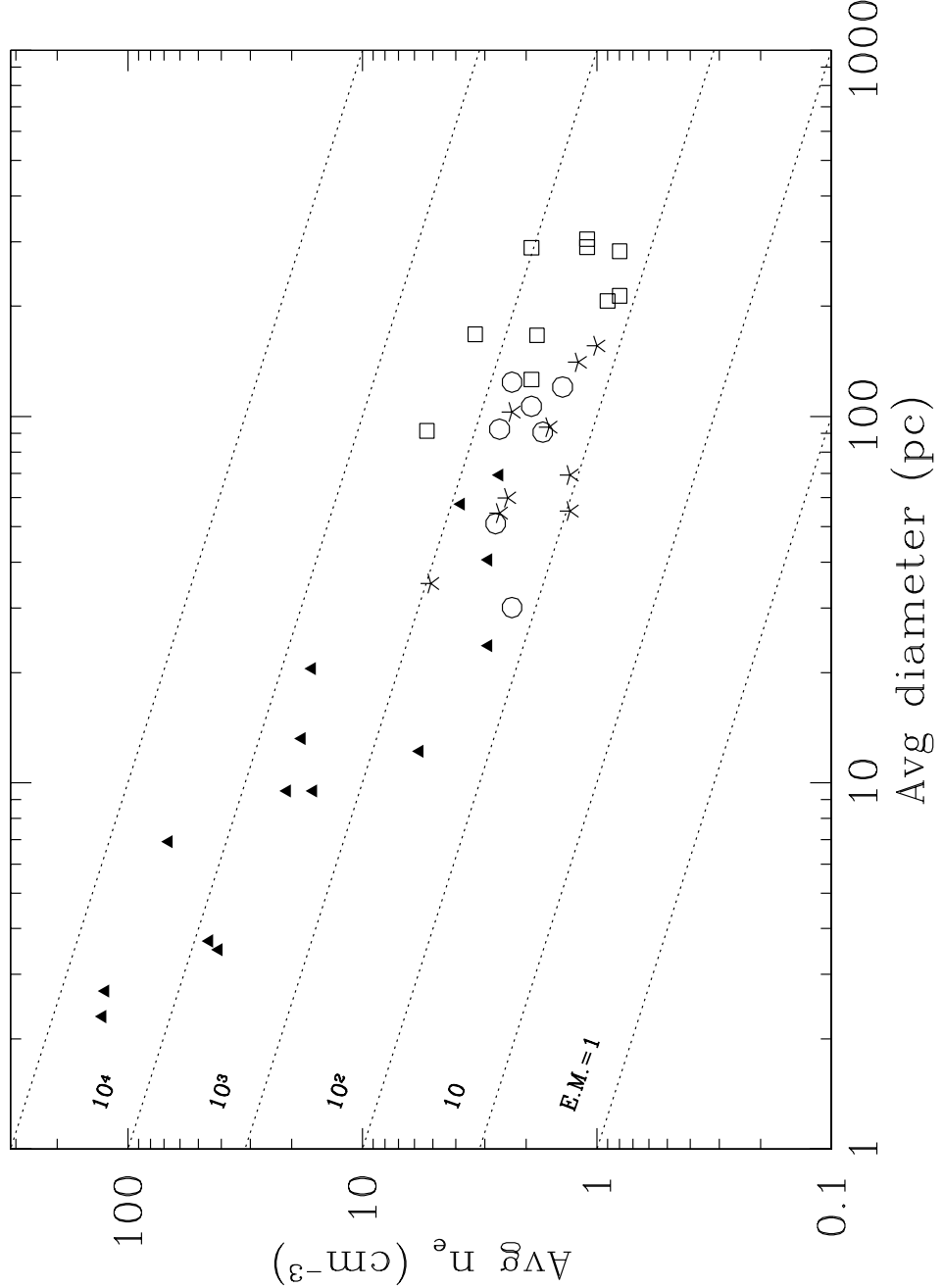


Fig. 3.— A comparison of the size distribution and electron densities of the HII regions in our sample. This figure shows average rms-electron density (estimated from the H α emission measures assuming unit filling factor) plotted against average nebular diameters. Dotted lines represent lines of constant emission measure in pc cm $^{-6}$. Point types specify morphological classification adopted from Walterbos & Braun (1992): center-brightened sources (triangles), ring-like nebulae (open circles), diffuse nebulae (stars) and complexes (open squares).

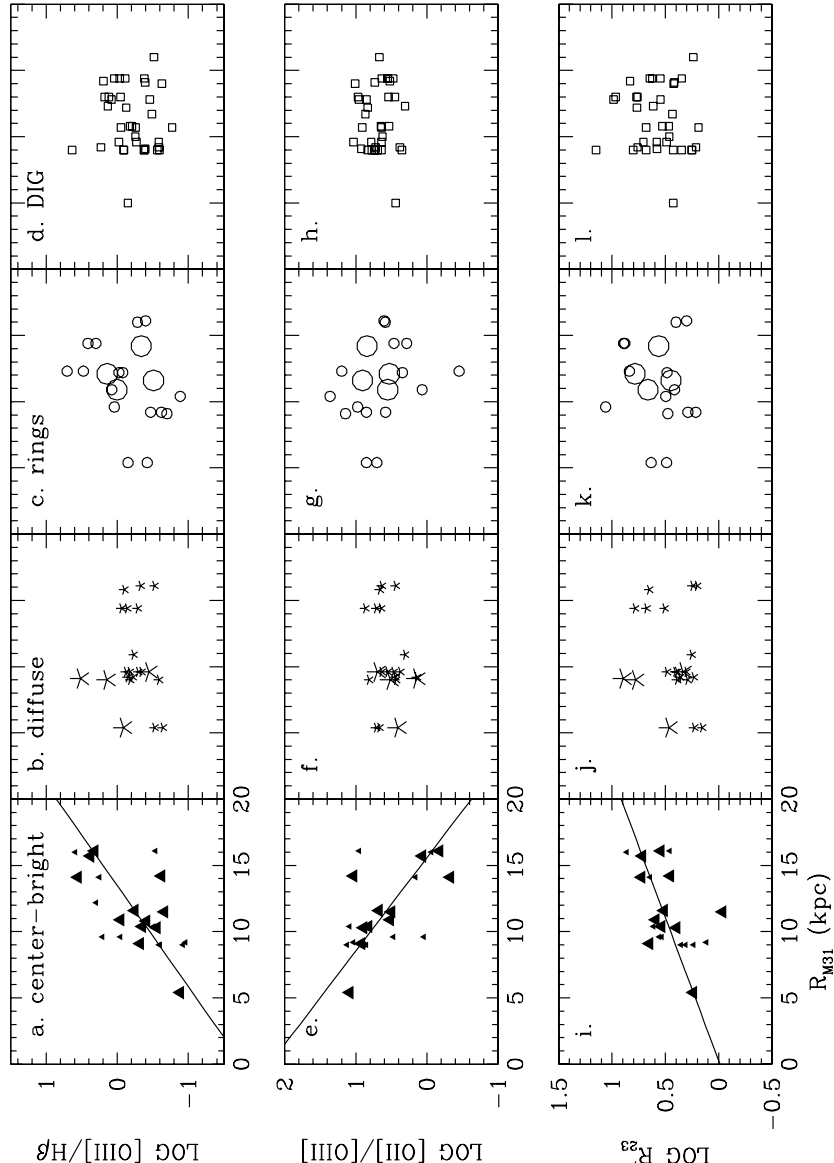


Fig. 4.— Radial distributions of the detected oxygen line ratios, $[OIII]/H\beta$ (**top row**), $[OII]/[OIII]$ (**middle row**), and R_{23} (**bottom row**) for HII regions and DIG. Panels demonstrate (*from left to right*) line variations with galaxy position for individual center-brightened nebulae and knots that are part of larger complexes (large and small triangles, respectively); for diffuse nebulae and diffuse sections of complexes (large and small stars, respectively); and for rings and arcs in complexes (large and small open circles, respectively). The regions of DIG are represented by open squares. Errorbars (not plotted) are approximately the size of the large points. Least squares linear fits are plotted here only for those cases where the correlation coefficient ≥ 0.5 . Radial gradients which are expected in these line ratios due to the chemical abundance gradient in the galaxy, only appear in the center-bright HII regions (left-most panels).

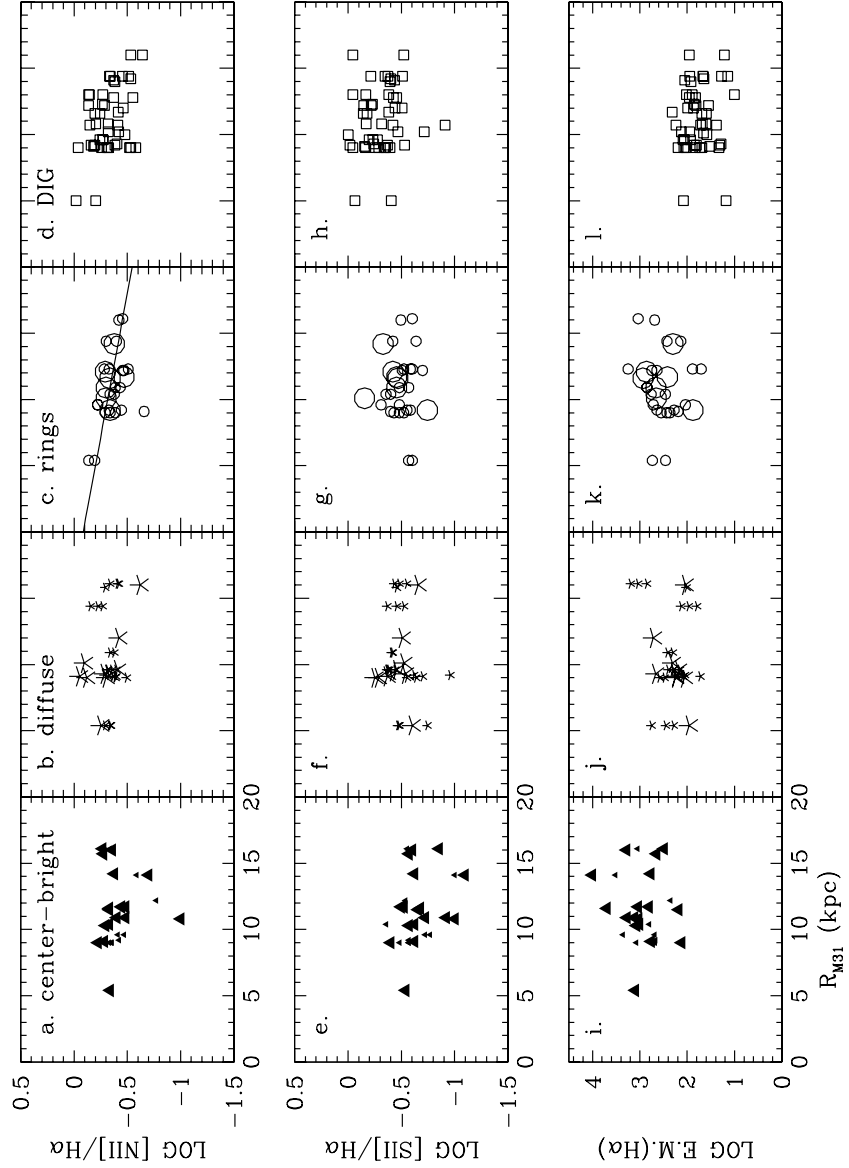


Fig. 5.— Radial distributions for the detected line ratios $[\text{NII}]/\text{H}\alpha$ (**top row**), $[\text{SII}]/\text{H}\alpha$ (**middle row**), and the $\text{H}\alpha$ emission measure obtained in each spectrum (**bottom row**) for HII regions and DIG. Point types and panels are the same as in Fig 4. The only significant linear correlation was found in the $[\text{NII}]$ emission of ring nebulae.

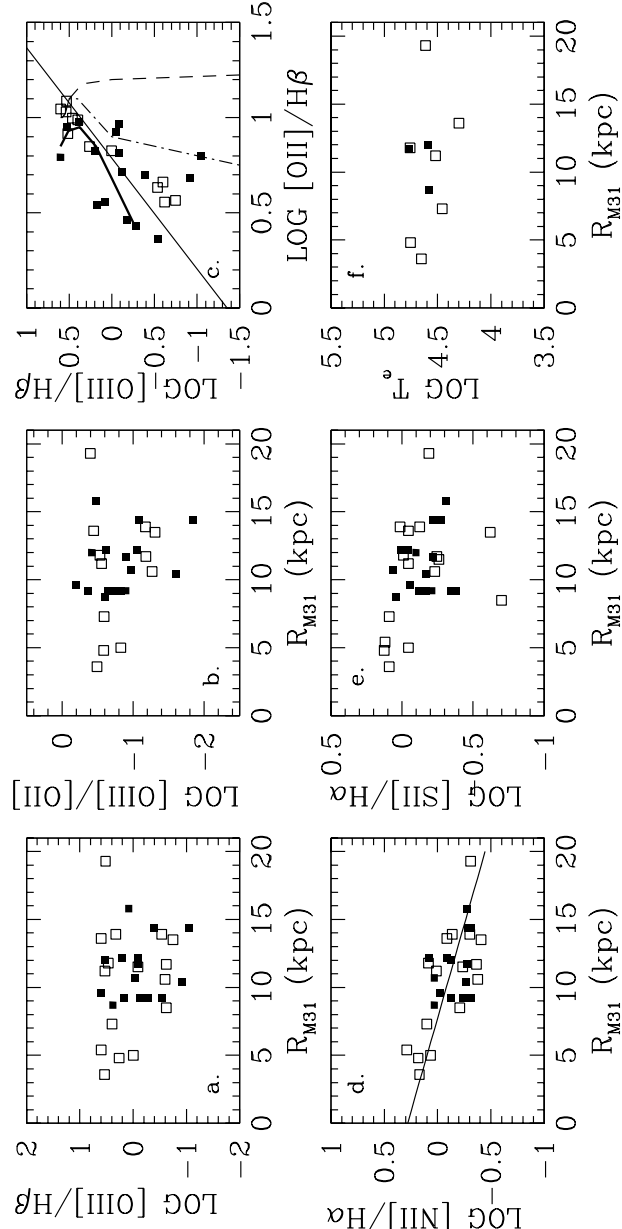


Fig. 6.— Radial distribution of line ratios and physical conditions for the confirmed SNRs from this paper (filled squares) and SNRs from Blair, Kirshner & Chevlier (1981, 1982) (open squares). Linear χ^2 fits are shown where applicable. **Top row:** radial variation in the line ratios (a) [OIII]/H β and (b) [OIII]/[OII], and the correlation between the [OIII] and [OII] emission in (c). Shock-ionization models from Dopita *et al.* (1984) are plotted as follows: dash-dot and dash curves show predictions for two models (standard and pre-ionized) for a range of shock velocity from 50 to 140 km sec $^{-1}$; thick solid curve shows the predicted effects on the [OII] and [OIII] emission for a variation in oxygen metallicity from N(O) = 2 x 10 $^{-3}$ (highest point) to 8 x 10 $^{-4}$. **Bottom row:** radial variation in the line ratios (d) [SII]/H α , (e) [NII]/H α , and the electron temperature determined from the [OIII] line ratio. Fits are plotted only for significant correlations as in previous plots.

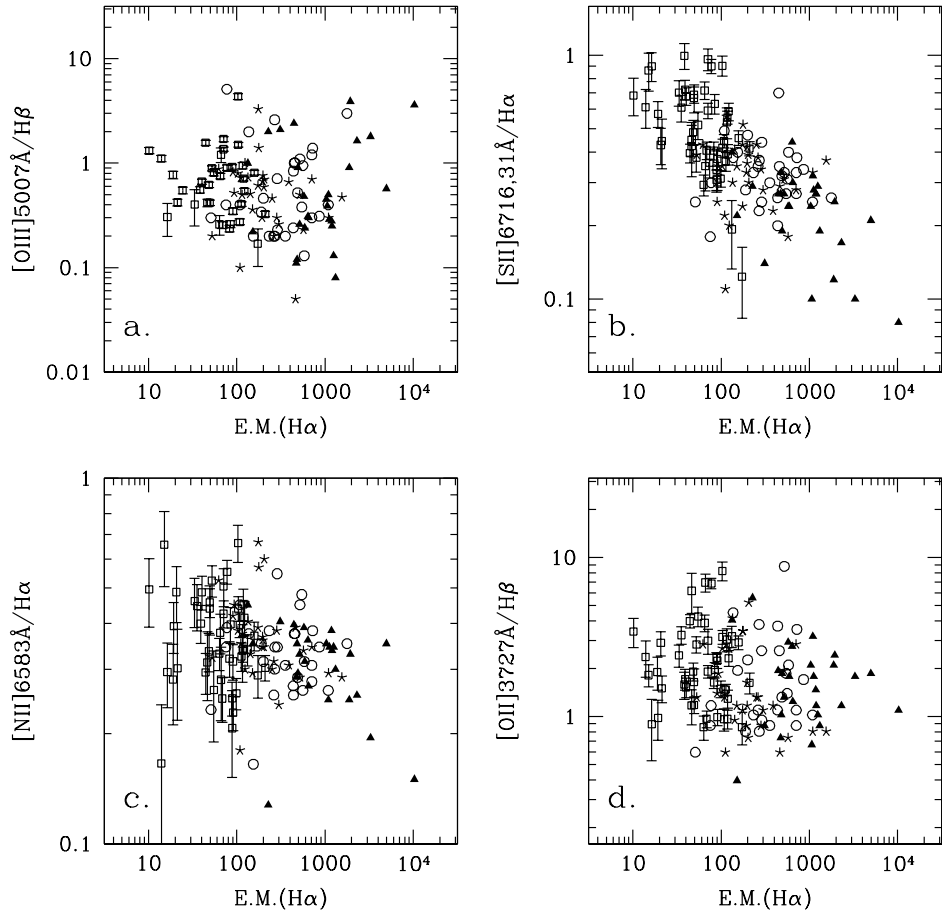


Fig. 7.— Line ratio variations with $\text{H}\alpha$ emission measure for HII regions and DIG. Point types are the same as in Fig 5. The errorbars have only been plotted for the DIG to minimize clutter; the errorbars on the HII region data are smaller.

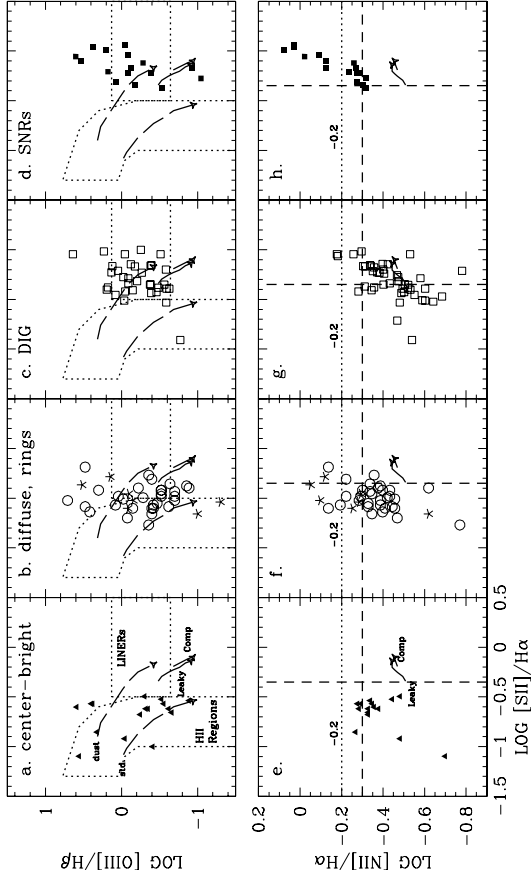


Fig. 8.— Diagnostic diagrams based on the [OIII], [NII], and [SII] emission in the various nebulae and DIG. **Top row:** Theoretical models from Shields & Filippenko (1990) are labelled as outlined boxes and separate photoionized objects (labelled “HII regions”) from shock-ionized objects (labelled “LINERs”). A smooth transition in [SII] emission links the brightest HII regions (leftmost panel), fainter HII regions, DIG and SNR (rightmost panel). Two photoionization models of Sokolowski (1993) shown as dashed lines are labeled “std” (standard model) and “dust” (dust-depletion model) in the first panel. The predictions of both models reproduce the increase in [SII] and decrease in [OIII] seen between the brightest HII regions and the DIG. The leaky HII region and composite photoionization models of Domgörgen & Mathis (1994) are also plotted as solid curves and labelled “Leaky” and “Comp”; the models are plotted from $\log(q)=-4$ to $\log(q)=-2$, where q is the ionization parameter as defined by Domgörgen & Mathis (1994). The arrows on the curves indicate the direction of decreasing ionization parameter. **Bottom row:** A comparison of the [SII] and [NII] emission properly distinguishes photoionized and shock-ionized objects. The two dashed lines delineate the limiting values which best separate the two ionization mechanisms: $[\text{SII}]/\text{H}\alpha=0.45$ and $[\text{NII}]/\text{H}\alpha=0.5$. Clearly, the confirmed SNRs lie in the upper right quadrant while the HII regions and DIG mostly lie outside of this region. Solid lines represent the two photoionization models of Domgörgen & Mathis (1994) as indicated above. The dotted line at $\log([\text{NII}]/\text{H}\alpha)=-0.2$ is a lower limit based on shock ionization models and is

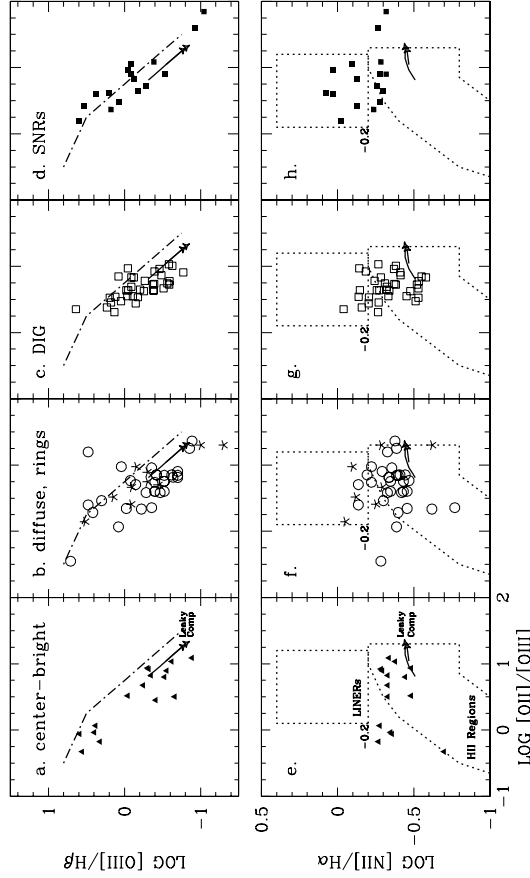


Fig. 9.— Diagnostic diagrams for various types of HII regions, DIG and SNRs in terms of [OIII], [NII], and the ionization line ratio [OII]/[OIII]. **Top row:** All HII region points lie below the upper envelope of theoretical photoionization models (Evans & Dopita, 1985) marked as the dash-dot curve. The SNR data lie mostly close to or above this curve while the DIG points lie beneath, indicating that the [OIII] emission from the DIG is consistent with photoionization. The photoionization models of Domgörgen & Mathis (1994) are also plotted and labelled as in Fig 8. **Bottom row:** [NII] emission relative to [OII]/[OIII] is also used to separate photoionization from shock-ionization; the outlined boxes represent Shields & Filippenko (1990) theoretical models for photoionized and shock-ionized gas. The HII region points fit mostly within the photoionization regime while the SNR close to or inside the shock ionization box. Many of the SNRs fall below the lower limits on the [NII] emission for shock ionization ($\log([NII]/H\alpha) = -0.2$); however, this is likely an abundance effect. These same data points have high [SII] consistent with shock ionization as shown in Fig 8h. Again the DIG points follow close along with the HII regions, demonstrating the [NII] emission from DIG is mostly consistent with photoionization.

This figure "Galarza.fig1a.jpg" is available in "jpg" format from:

<http://arxiv.org/ps/astro-ph/9908271v1>

This figure "Galarza.fig1b.jpg" is available in "jpg" format from:

<http://arxiv.org/ps/astro-ph/9908271v1>